Upper mantle seismic structure beneath eastern Mexico determined from P and S waveform inversion and its implications

Wei Gao,[1] Eric Matzel,[2] and Stephen P. Grand[1]

Received 20 January 2006; revised 16 April 2006; accepted 9 May 2006; published 24 August 2006.

[1] We present compressional (P) and shear (S) wave seismic velocity models for the upper mantle beneath southeastern Mexico derived from waveform inversion of triplicated seismic phases. The seismic waveform data produced by an earthquake located near the Mexico-Guatemala border were recorded by the La Ristra passive seismic array. The La Ristra seismic array consists of 54 broadband seismometers arranged linearly from west Texas to southeastern Utah. The orientation of the La Ristra array is nearly along the great circle from the event, and the distance (18.5°–26.5°) of the seismic array from southern Mexico is such that the data are ideal for investigating localized seismic structure of the upper mantle. Previous tomography and receiver function studies provide a priori knowledge of receiver-side crustal and upper mantle structure from which static adjustments were made to the seismic data. The waveforms were inverted for mantle velocity from 40 to 1000 km depth using a conjugate gradient algorithm. In the inversion, we evaluated a suite of starting models with different depths of the 410 km and 660 km discontinuities and varying velocity gradients. The best fitting models have velocity increases across the 410 km discontinuity of 6.2% and 7.3% for P and S wave velocities, respectively. The velocity jump across the 660 km discontinuity was found to be 3.3% for P waves and 6.3% for S waves. The size of the upper mantle discontinuities that we find are more in agreement with a pyrolite composition than standard reference models imply. A common feature of the best fitting models is a low-velocity zone above the 410 km discontinuity that is more prominent in the shear velocity model than the compressional velocity model. This feature may be due to partial melting induced by water release from the transition zone. The overall jump in velocity at 410 km is also larger than in previously published models with a lower gradient below. In addition, the P wave data require a small discontinuity at 490 km depth that is not resolved in the S data. Finally, the S wave data require an unusually high gradient beginning at about 600 km depth extending to the 660 km discontinuity. This feature may be due to a thermal and/or mineralogic anomaly due to a flat lying slab beneath eastern Mexico.

Citation: Gao, W., E. Matzel, and S. P. Grand (2006), Upper mantle seismic structure beneath eastern Mexico determined from P and S waveform inversion and its implications, *J. Geophys. Res.*, *111*, B08307, doi:10.1029/2006JB004304.

1. Introduction

[2] The seismic structure of the upper mantle is a fundamental constraint for understanding the mineral and chemical composition of the mantle as well as the dynamics of the Earth. Compressional and shear wave velocities are sensitive to temperature variations, melt content, mineralogy, and chemical composition and provide our most direct observations of these properties in the mantle below about 200 km depth. Seismic observations have shown that the upper mantle is highly variable laterally but that there are features common to most regions. In particular, there are two significant and ubiquitous seismic velocity discontinuities in the upper mantle, the 410 km and 660 km discontinuities, which form the boundaries of the transition zone in the upper mantle. It is believed that the 410 km discontinuity results from a phase transition of olivine to the wadsleyite structure and the 660 km discontinuity is caused by the dissociation of ringwoodite to perovskite and magnesiowüstite [e.g., *Bina and Helffrich*, 1994]. Recent seismic observations also indicate that there may be a small global discontinuity near 520 km depth [*Shearer*, 1990; *Tajima and Grand*, 1995, 1998; *Ryberg et al.*, 1997; *Simmons and Gurrola*, 2000; *Deuss and Woodhouse*, 2001; *Helffrich et al.*, 2003] that may represent an intermediate phase transition from the wadsleyite to ringwoodite structure [*Sinogeikin et al.*, 2003; *Li*, 2003]. Other minerals also go through phase changes with depth in the upper mantle leading to high gradients and other possible jumps in

[1] Jackson School of Geosciences, University of Texas at Austin, Austin, Texas, USA.
[2] Lawrence Livermore National Laboratory, Livermore, California, USA.

0148-0227/06/2006JB004304$09.00

Table 1. Event Parameters

Parameter	Value
Date	19 Jan 2001
Time	0112:55.8
Latitude	15.33°N
Longitude	92.93°W
Depth	83 km
Magnitude	5.4 M_b
Strike	140°
Dip	13°
Slip	−91°

seismic velocity. Adding to the complexity in interpreting seismic models is that the pressure at which phase changes occur changes with temperature, chemical heterogeneity and water content [*Bina and Wood*, 1984; *Flanagan and Shearer*, 1998].

[3] A commonly used model for the composition of the upper mantle is pyrolite. The pyrolite model was developed by *Ringwood* [1975] and its primary mineralogic constituents are olivine (57% by weight) with less common clinopyroxene, orthopyroxene, and garnet. As mentioned above, the phase changes that the olivine portion of the upper mantle undergoes are thought to explain the jumps in velocity near 410 and 660 km depth, respectively. In theory, if mineral physics experiments can determine the seismic velocity jumps associated with the olivine to wadsleyite phase change and the ringwoodite to perovskite and magnesiowüstite dissociation then the observed seismic velocity jumps near 410 and 660 km depth can be used to infer the olivine content of the mantle. *Bass and Anderson* [1984] compared the best mineral physics prediction of seismic velocity associated with the pyrolite model to published seismic models and found the pyrolite model did not fit the seismic models. They found a better fit was obtained with an upper mantle composition containing only 16% olivine and far more clinopyroxene than in the pyrolite model. Their results were controversial at the time [*Bina and Wood*,

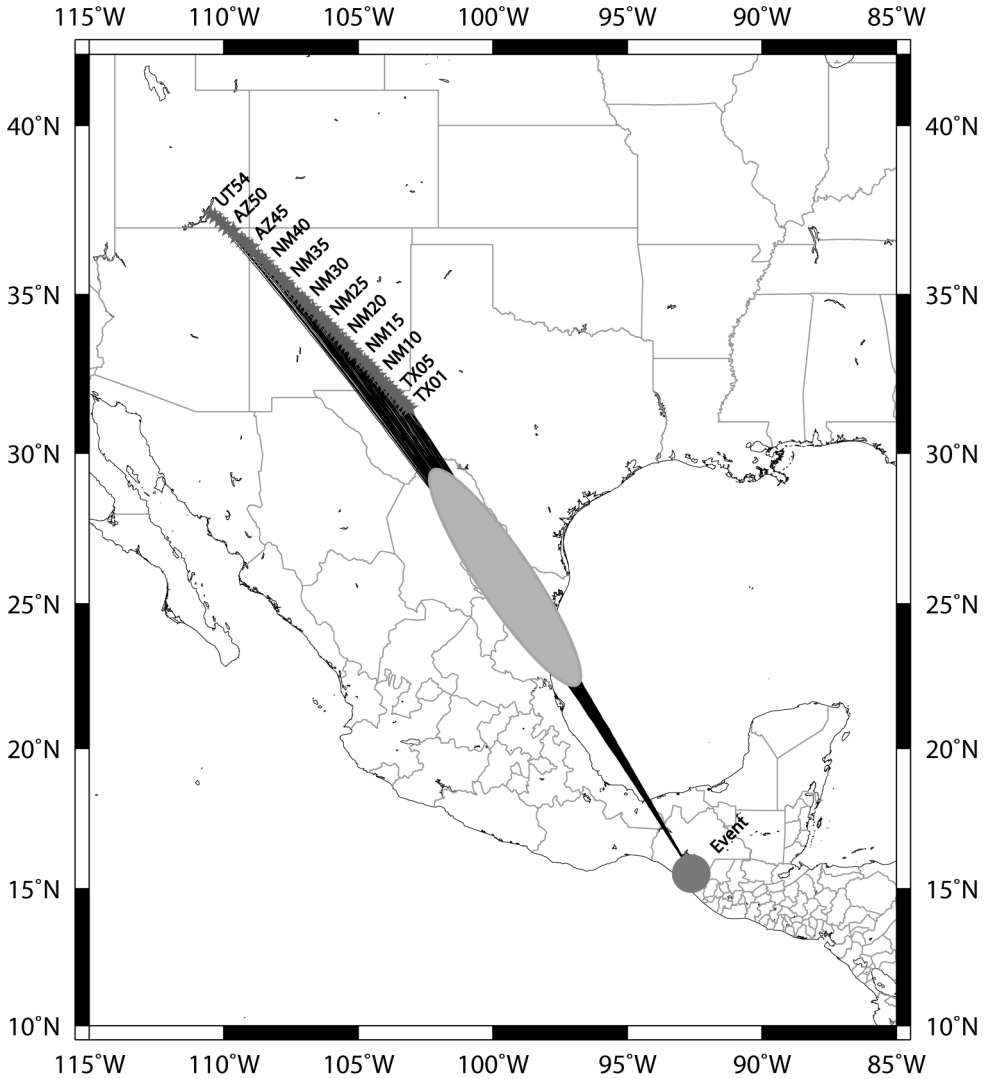

Figure 1. Map of the location of the La Ristra array seismic stations and the earthquake used in this study. The great circle paths between the event and stations are also showed. The ellipse presents the area where the waves turn and thus sample the transition zone.

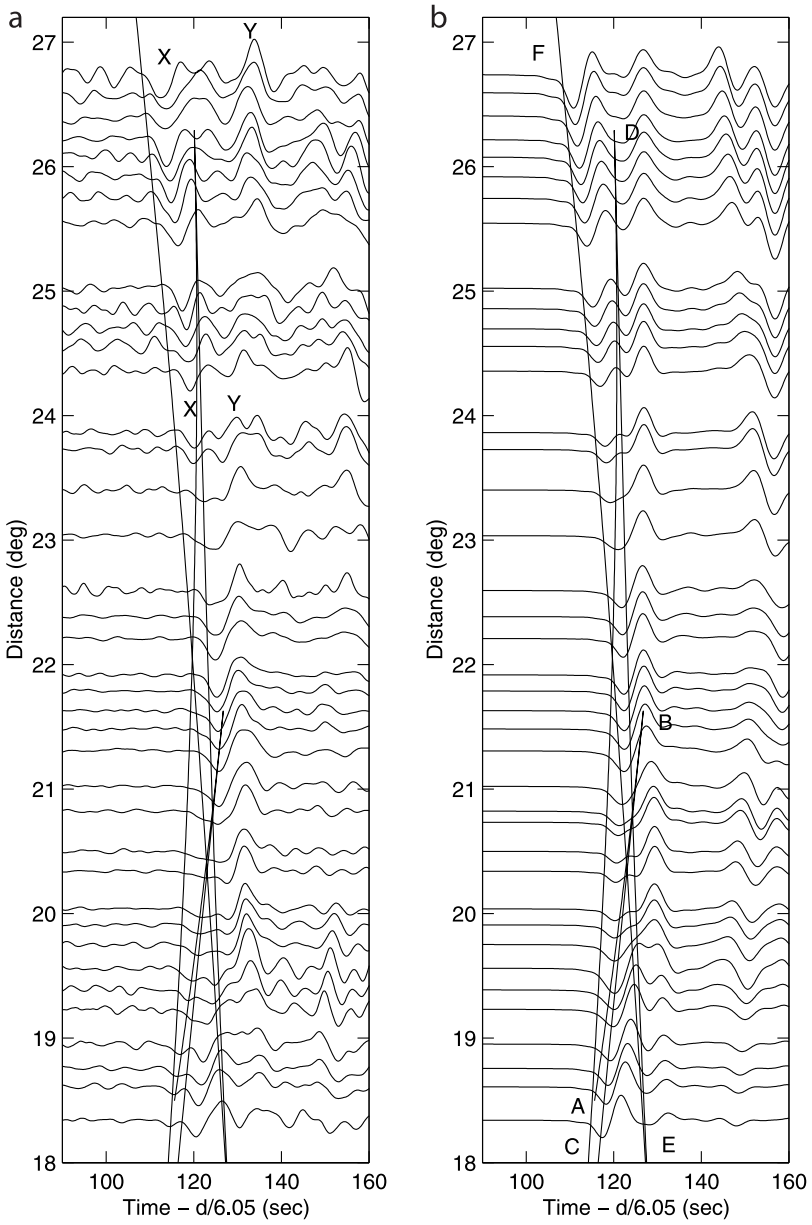

Figure 2. (a) Tangential component seismograms and (b) synthetics calculated from the IASPEI model. The IASPEI predicted traveltime curves are overlaid on both the data and synthetics. The timescale is shown with a reduction velocity of 6.05 km s^{-1}, where d is epicentral distance in km.

1987; *Weidner*, 1985], but a more recent comparison of mineral physics predictions of the pyrolite model versus published seismic models by *Li et al.* [1998] has found that, indeed, the pyrolite model does not produce an acceptable fit to standard seismic models of the upper mantle. *Li et al.* [1998] go further and state that no single chemical composition of the mantle satisfies the seismic profiles over the depth range 400 to 650 km. *Cammarano et al.* [2005] have reexamined the consistency of a pyrolite upper mantle with seismic constraints. The seismic constraints used in their study are a global set of P and S traveltimes as well as the periods of the free oscillations of the Earth. They also use a range of different mineral physics parameters and find a small subset of mineral physics parameters that predict seismic velocities consistent with the seismic data for a pyrolite composition.

[4] It is clear that better constrained mineral physics measurements of bulk and shear moduli of high-pressure mineral phases will be necessary to uniquely determine upper mantle composition. However, given the strong lateral variations in temperature and possibly composition within the upper mantle, it will also be necessary to determine upper mantle P and S velocity structure within specific regions to compare directly to mineral physics predictions. Commonly, reference seismic models like PREM [*Dziewonski and Anderson*, 1981] or AK135

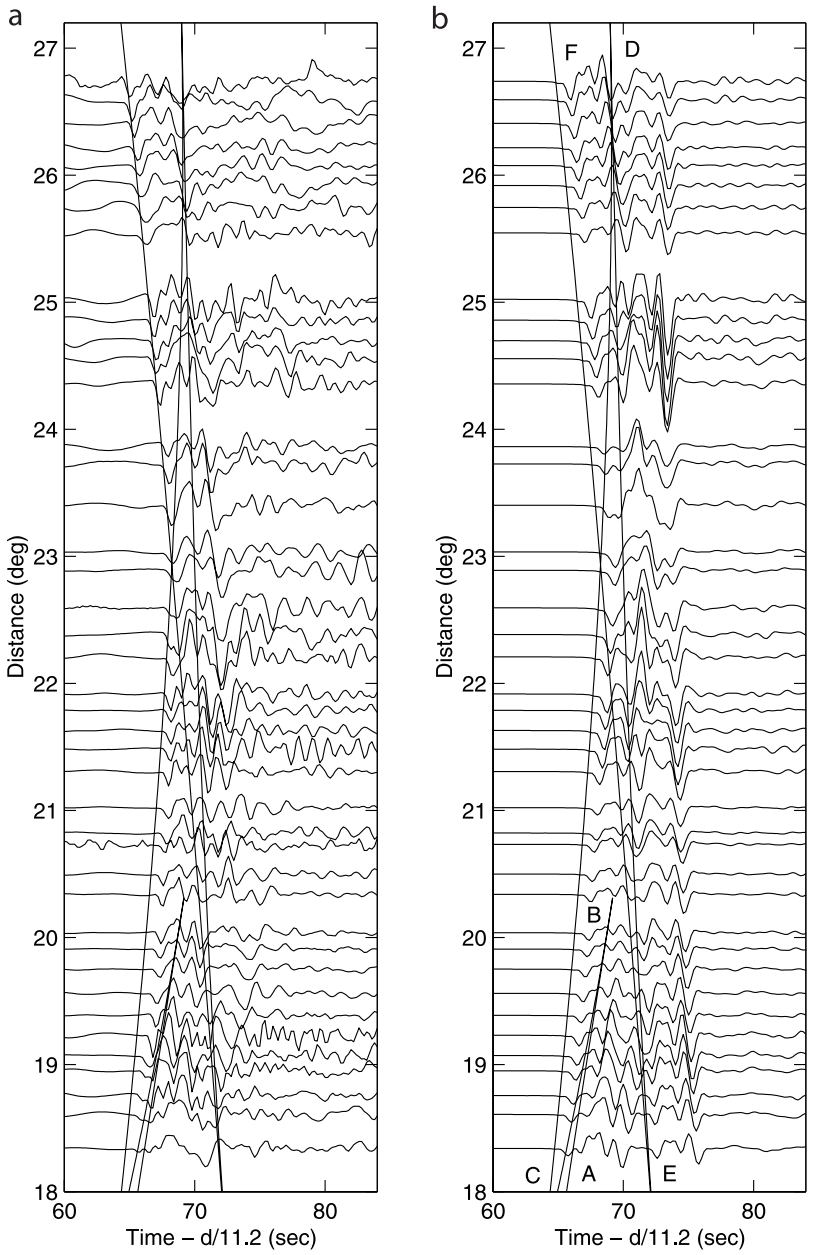

Figure 3. (a) Vertical component seismograms (P waves) and (b) synthetics calculated from the IASPEI model. The IASPEI predicted traveltime curves are overlaid on both the data and synthetics. The timescale is shown with a reduction velocity of 11.2 km s^{-1}, where d is epicentral distance in km.

[*Kennett et al.*, 1995] are used for comparison to mineral physics predictions. These models satisfy the traveltimes of a global set P and S data and thus have large error bars as well as little resolution of the details of discontinuity structure and gradients. Global tomography is a powerful tool to image three-dimensional seismic velocity variations but resolution is still quite limited (see *Romanowicz* [1991] for a review) and detailed gradients and discontinuity structure are still not available from such techniques. The use of underside reflected precursors of SS and PP waves [*Shearer and Flanagan*, 1999; *Gu et al.*, 2003] or converted Ps or Sp waves have also been powerful techniques to investigate the upper mantle seismic structure. These type studies provide strong constraints on topography of upper mantle discontinuities and the impedance contrast across the discontinuities. Although it is possible to determine the velocity jump across the discontinuity by using the amplitude versus angle of incidence of reflected or converted waves, there are usually high uncertainties in the results. Also, these techniques provide no information on velocity gradients between discontinuities. The data most sensitive to seismic velocity as a function of depth in the upper mantle are P and S waves that turn within the upper mantle. The discontinuities within the upper mantle produce tripli-

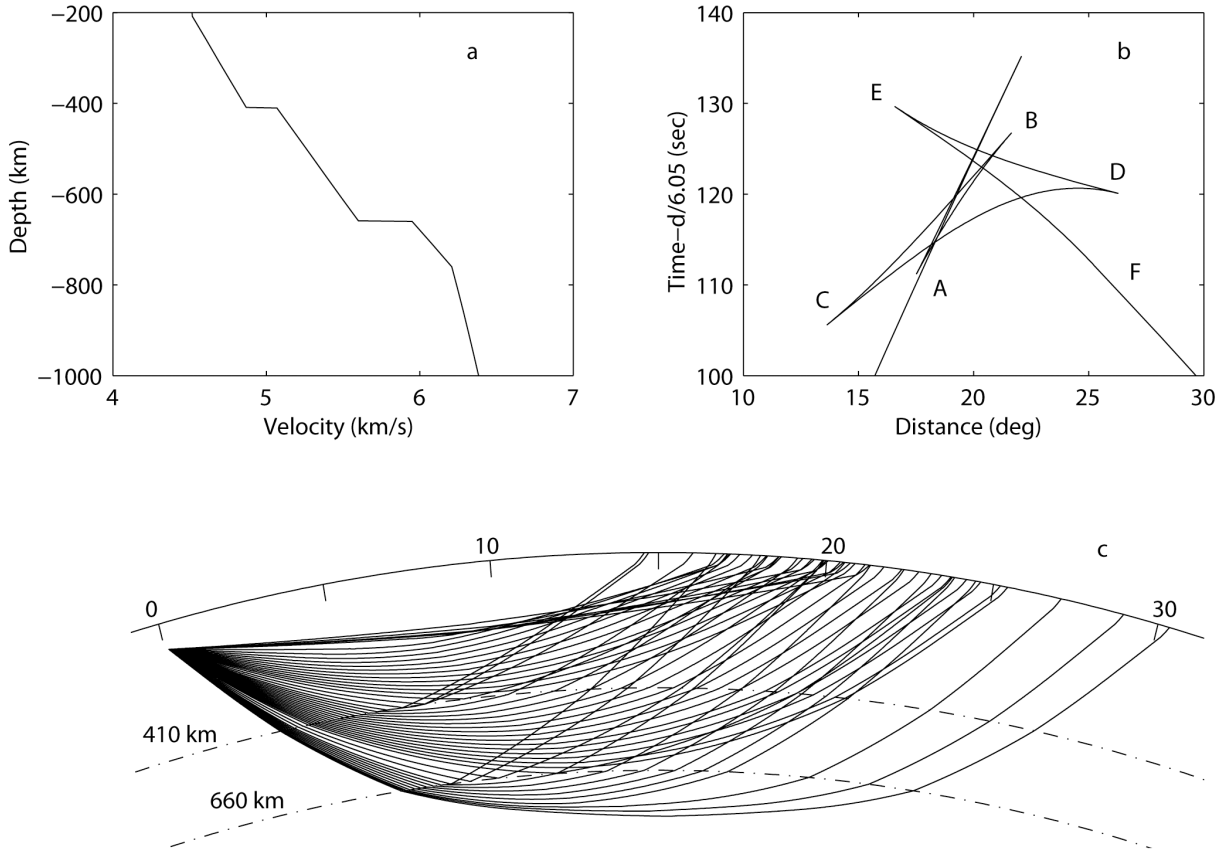

Figure 4. (a) IASPEI shear velocity model. (b) Traveltime curve for the IASPEI shear velocity model for a source at 80 km depth. The timescale is shown with a reduction velocity of 6.05 km s^{-1}, and d is epicentral distance in kilometer. (c) Ray paths for the IASPEI shear velocity model.

cations for these waves and thus complicated waveforms but these complications can be used to place tight constraints on velocity variations with depth [*Walck*, 1984; *Grand and Helmberger*, 1984; *Nolet et al.*, 1994].

[5] Upper mantle turning waves have yielded detailed models of the transition zone; however, they are often constructed by trial-and-error with a nonideal source receiver distribution and few are generated with compressional and shear waves that are produced by the same earthquakes. Hence the resolution that these seismic models provide of the upper mantle is difficult to assess. Another problem is that a one-dimensional (1-D) model is extracted from data that actually sample fully three dimensional structures and it has been difficult to assess the effects of the 3-D variations on the model. In this paper we use a waveform inversion technique applied to an optimal data set of P and S upper mantle turning waves generated from one earthquake to derive 1-D P and S velocity models of the transition zone beneath eastern Mexico. The waveform inversion approach overcomes the deficiency of the trial-and-error modeling by producing an optimal data fit with some a priori constraints. The data set we use is also ideal in that it consists of a densely spaced line of broadband seismic recordings aligned with the great circle path from the earthquake source. Finally, P and S tomography inversions have been conducted beneath the array so there is some constraint on the lateral variations in velocity sampled by the data.

2. Data and Observations

[6] The Colorado Plateau, Rio Grande Rift, and Great Plains Seismic Transect (La Ristra) experiment consisted of 54 broadband seismometers deployed from August 1999 to May 2001. The stations were deployed in a line beginning in west Texas, crossing the Rio Grande rift and ending in the center of the Colorado Plateau spanning about 950 km [*Gao et al.*, 2004]. In this paper we used Ristra data produced by an earthquake occurring near the border between Guatemala and Mexico (see Table 1). The Ristra array spanned 18.5 to 26.5 degrees in distance along the surface from the earthquake epicenter and the orientation of the array was approximately along a great circle with the event source (Figure 1). This makes these data ideal for investigating the detailed seismic structure in the transition zone of the upper mantle beneath eastern Mexico. We searched for other earthquakes in the same region but the January 19, 2001 event was the only one that produced both clear P and S waves. The earthquake depth is 82 km resulting in upgoing pP and sS waves arriving later than the triplicated arrivals from the transition zone. Figure 2a shows the Ristra S wave recordings (tangential component), and Figure 2b shows

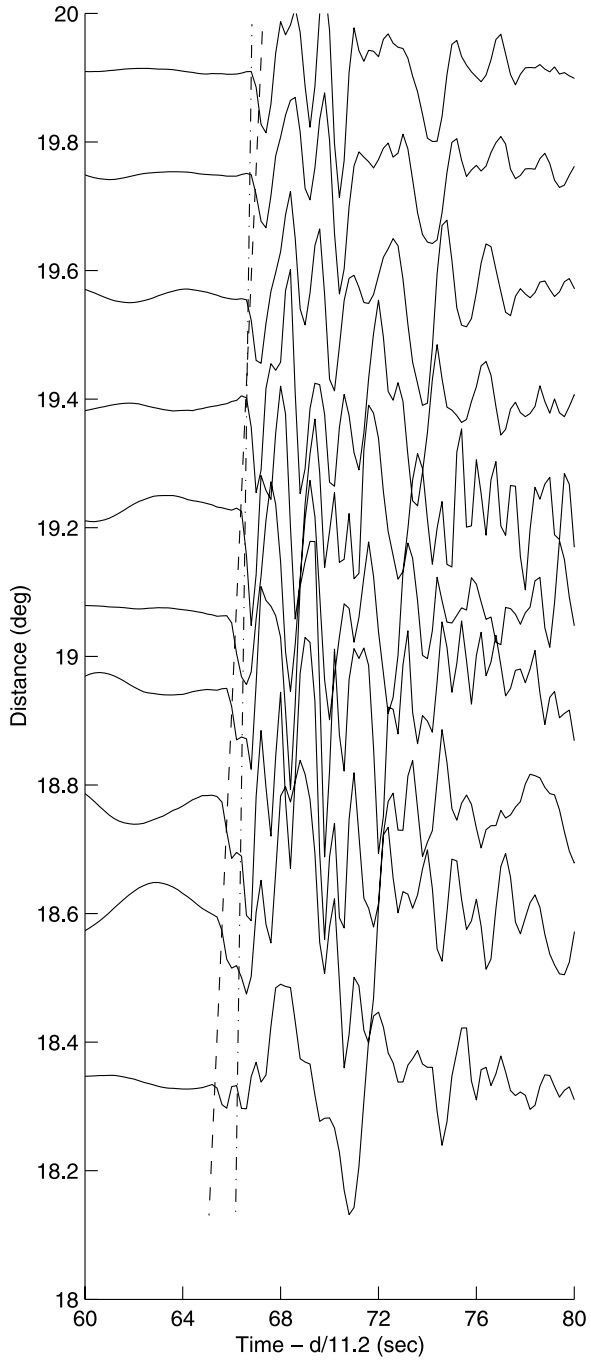

Figure 5. Vertical component data from 18° to 20° distance. The dashed and dash-dotted lines show two arrivals that progressively come together with distance. The timescale is shown with a reduction velocity of 11.2 km s^{-1}, where d is epicentral distance in km.

synthetic seismograms computed using the IASP91 [*Kennett and Engdahl*, 1991] shear velocity model. The synthetics were computed using the reflectivity technique [*Fuchs and Muller*, 1971]. The seismograms in Figure 2a were band-pass filtered from 0.01 to 0.25 Hz. Figures 3a and 3b show the P wave data (vertical component) and P wave synthetics computed using the IASP91 model. The P wave data were band-pass filtered from 0.01 to 1.5Hz. The observed seismograms were shifted in time to account for topography and crustal thickness variations along the line such that the arrival times of the data should correspond to those expected for a 35 km thick crust with zero topography. We used the crustal model of *Wilson et al.* [2005] and ray parameters predicted by the IASP91 model to make the corrections. *Gao et al.* [2004] inverted P and S data recorded by Ristra stations and produced P and S tomography velocity models of the upper mantle beneath the array. This model has significant heterogeneity in the upper 200 km of the mantle beneath the array. To account for this, we traced rays using the IASP91 model from the earthquake to the array and calculated the relative timing shifts due to the shallow heterogeneity beneath the stations. The data, both P and S, were shifted to account for these timing variations due to shallow mantle lateral heterogeneity.

[7] In shear wave global tomography models [*Grand*, 2002; *Masters et al.*, 2000; *Megnin and Romanowicz*, 2000; *Gu et al.*, 2003; *Ritsema et al.*, 1999] the transition zone shows no significant structure. The regional study of *Van der Lee and Nolet* [1997], however, shows slightly faster shear velocity than average beneath eastern Mexico. They interpret the anomaly as due to remnants of the subducted Farallon plate. The anomaly in their model is small, however, and does not show significant lateral variations suggesting we can treat the transition zone in this study as a one dimensional structure.

[8] At the distances shown in Figures 2 and 3 actually S and P waves interact with upper mantle discontinuities resulting in triplicated waveforms. Figure 4 shows the S wave IASP91 model as well as the ray paths and traveltime curves predicted by the model for upper mantle distances. The IASP91 P model predicts triplicated arrivals similar to those predicted for S. Branch AB represents arrivals that turn above the 410 km discontinuity. Branch CD represents arrivals turning within the transition zone from 410 to 660 km depth. Finally, branch EF corresponds to waves that have turned below the 660 km discontinuity. The time separation of different branches with distance is most sensitive to the overall velocity increase across the respective discontinuity. We plot the IASP91 traveltime curves on the data in Figure 2. Clear multiple arrivals are seen in the data in Figure 2a. For example, arrivals labeled x and y in Figure 2a can be seen to separate with distance. The IASP91 model predicts two arrivals separating with distance but note that in the data the arrivals separate much faster than IASP91 predicts. Multiple arrivals are also clearly seen at closer distances in the S wave data, but although the IASP91 model predicts multiple arrivals at those distances, the predicted relative timing is off and thus the waveforms appear quite different.

[9] The compressional wave seismograms (Figure 3a) appear more complex than the S wave data. This is primarily due to the source mechanism of the earthquake as well as the intrinsically higher frequency of the P data than the S data. The P waves in Figure 3a are near nodal for the Harvard mechanism given in Table 1 and the subevents producing the P waves actually change polarity (not clear in the data). The SH waves are in the center of the radiation pattern and the source subevents are all of the same polarity. At longer periods noise dominates the vertical components. Beyond 26° there are no large secondary P phases due to

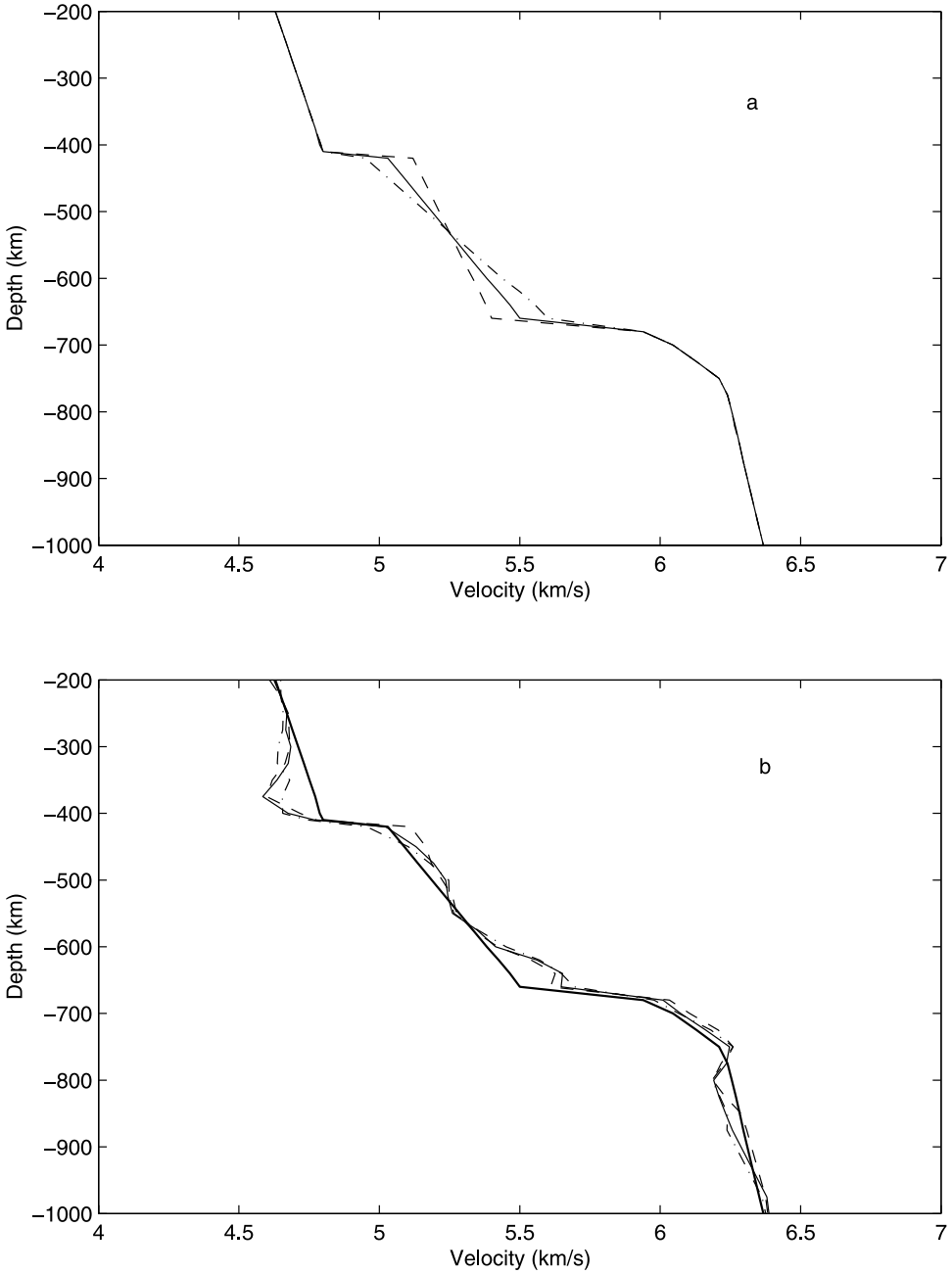

Figure 6. (a) Three starting shear velocity models used in an inversion of the tangential component data. (b) Results of inversion using the three models in Figure 6a. The heavy black line shows the starting model with the intermediate velocity gradient. The solid line shows the starting model and the inverted model with the intermediate velocity gradient, the dash-dotted line shows the starting model and the inverted model with the high-velocity gradient, and the dashed line shows the starting model and the inverted model with the low-velocity gradient.

upper mantle discontinuities and thus the seismograms at those distances in Figure 3a essentially represent the P wave source. We modeled the waveforms at the largest distances in the array to determine the source function used in the synthetics (Figure 3b). Despite the complicated source for the P waves, triplicated arrivals are apparent in the data. Figure 5 shows seismograms over a 2° distance range. Note the two pulses that at short distance are clearly distinct but cross at larger distance. IASP91 does not predict this behavior but a small jump in velocity near 500 km depth will produce a similar pair of arrivals that cross near 19° distance. At other distances careful analysis shows other multiple arrivals in the P data due to the upper mantle triplications, although the arrivals are more subtle than for the SH waves. Also it can be seen in Figure 3b that the predicted traveltimes of branch CD are earlier than the data at stations between 18 and 21 degrees in distance but are in agreement or later beyond 21° distance. Branch CD represents waves that are turning within the transition according to the IASP91 model. These observations and interpretations

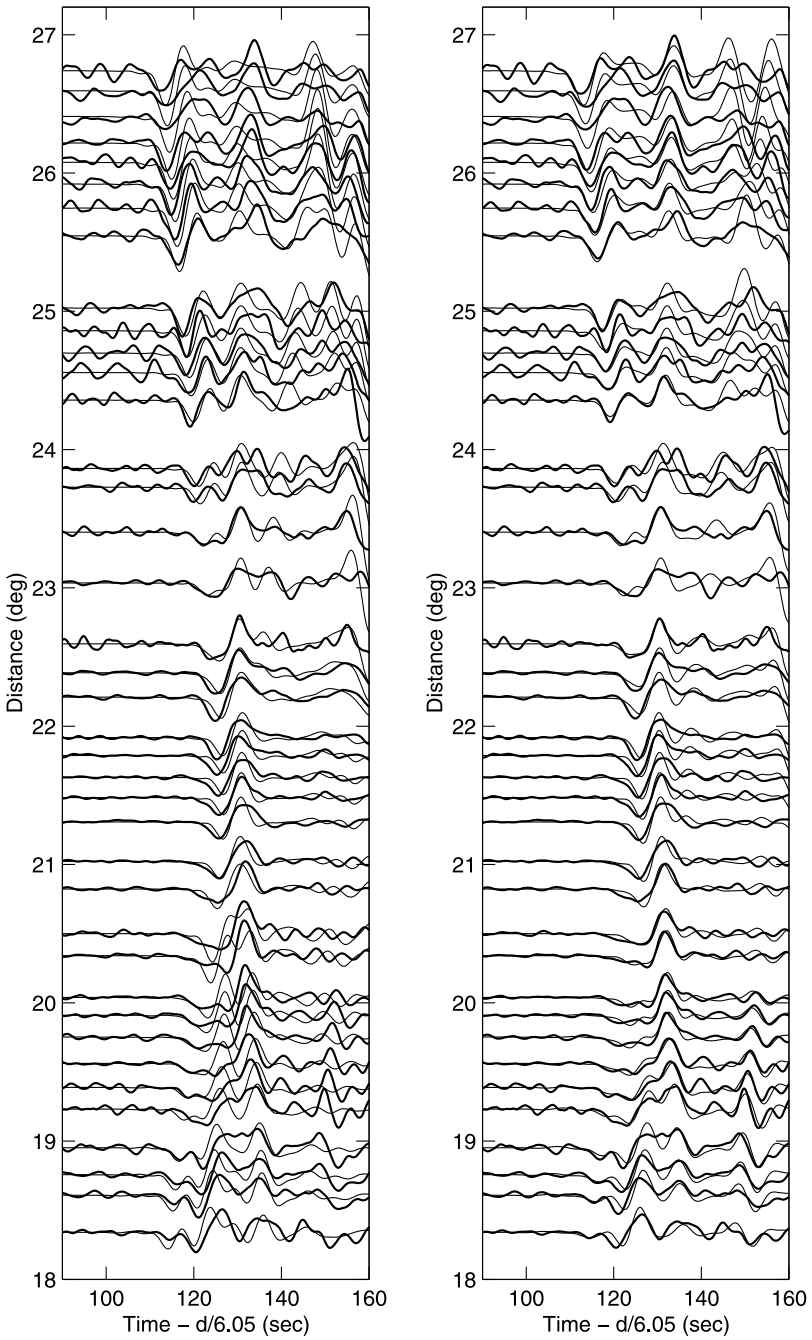

Figure 7a. Data and synthetics before and after inversion for the starting model in Figure 6a with a high gradient in the transition zone. (left) Synthetics computed using the starting model and (right) synthetics computed using the inverted model. The heavy black lines show the data. The timescale is shown with a reduction velocity of 6.05 km s^{-1}, and d is epicentral distance in km.

reveal significant differences in velocity in the transition zone beneath eastern Mexico relative to the IASP91 reference model.

[10] The seismic waveforms discussed above clearly show all the triplicated branch arrivals due to the upper mantle discontinuities for both P and S waves. It is clear that IASP91 does not match the relative timing of arrivals and thus the waveforms. IASP91 does match the first arrival times reasonably well, although there is a clear discrepancy for the P waves at the shorter distances. Other global average models such as PREM and AK135 also do a poor job of fitting the data. The data shown in Figures 2 and 3 are most sensitive to seismic velocity within the transition zone. If the shallower mantle is slower or faster than IASP91 the result would be primarily a shift in traveltime and the misfits in waveform would not be as large as seen. To determine the seismic P and S velocity structure of the transition zone beneath eastern Mexico, we used a waveform inversion technique developed by *Matzel and Grand* [2004] to invert

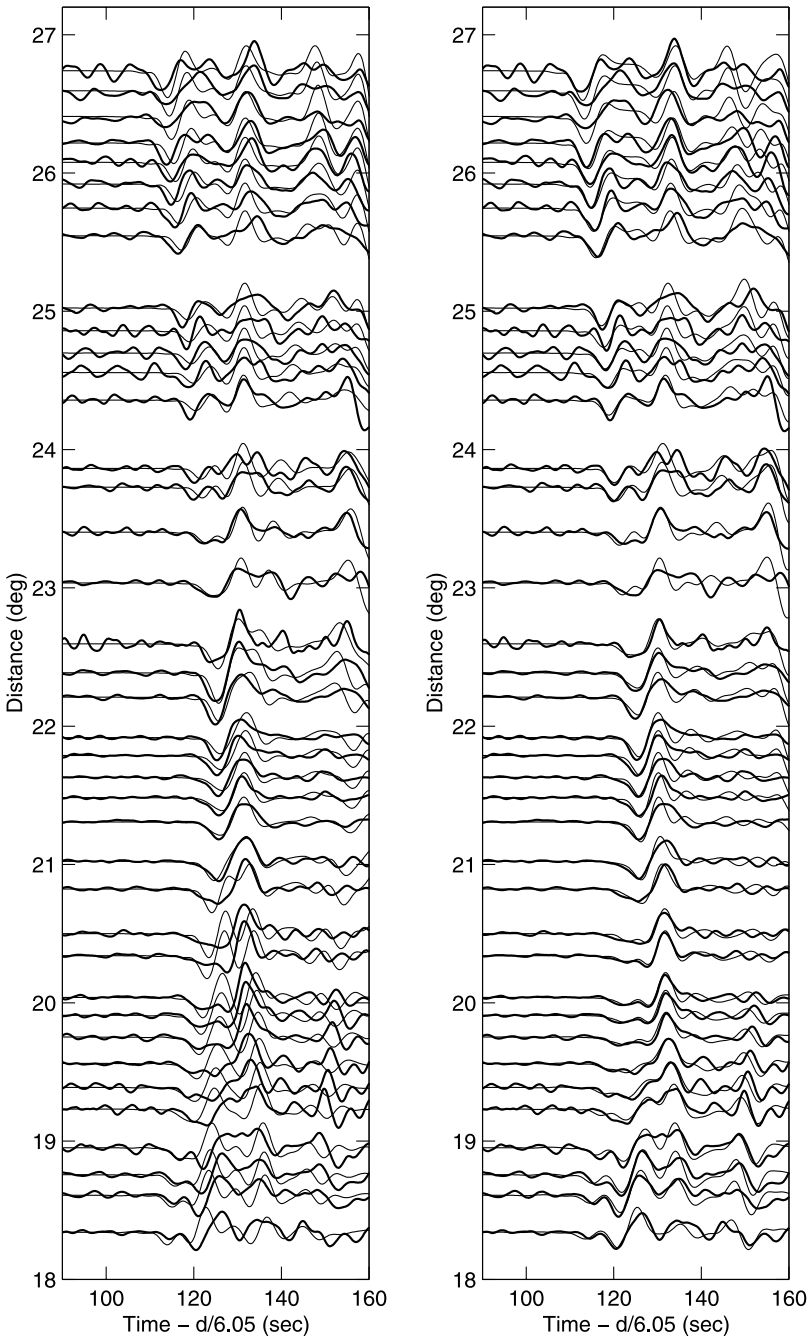

Figure 7b. Same as Figure 7a except the starting model was the intermediate gradient model in Figure 6a. The heavy black lines show the data. The timescale is shown with a reduction velocity of 6.05 km s^{-1}, and d is epicentral distance in km.

the data shown in Figures 2a and 3a. The technique is discussed in section 3.

3. Inversion

[11] The general nonlinear forward model for a seismic waveform synthetic can be written as

$$\mathbf{d} = f(\mathbf{m}, r_{\text{inst}}, r_{\text{source}}) \tag{1}$$

where **d** is the seismic synthetic vector, **m** is an Earth model vector, and f is a nonlinear operator that maps the model space M into the data space D and r_{inst} and r_{source} are instrument response and source information (mechanism and time function), respectively. Our objective is to find a model **m** that best fits the seismic observations by minimizing the difference between synthetic and observed waveforms. Here we briefly describe the inversion method. To linearize the nonlinear problem, we can write the relation

$$\mathbf{d}(\mathbf{m}, r_{\text{inst}}, r_{\text{source}}) - \mathbf{d}_{\text{obs}} = f(\mathbf{m}, r_{\text{inst}}, r_{\text{source}}) - f(\mathbf{m}_0, r_{\text{inst}}, r_{\text{source}}) \tag{2}$$

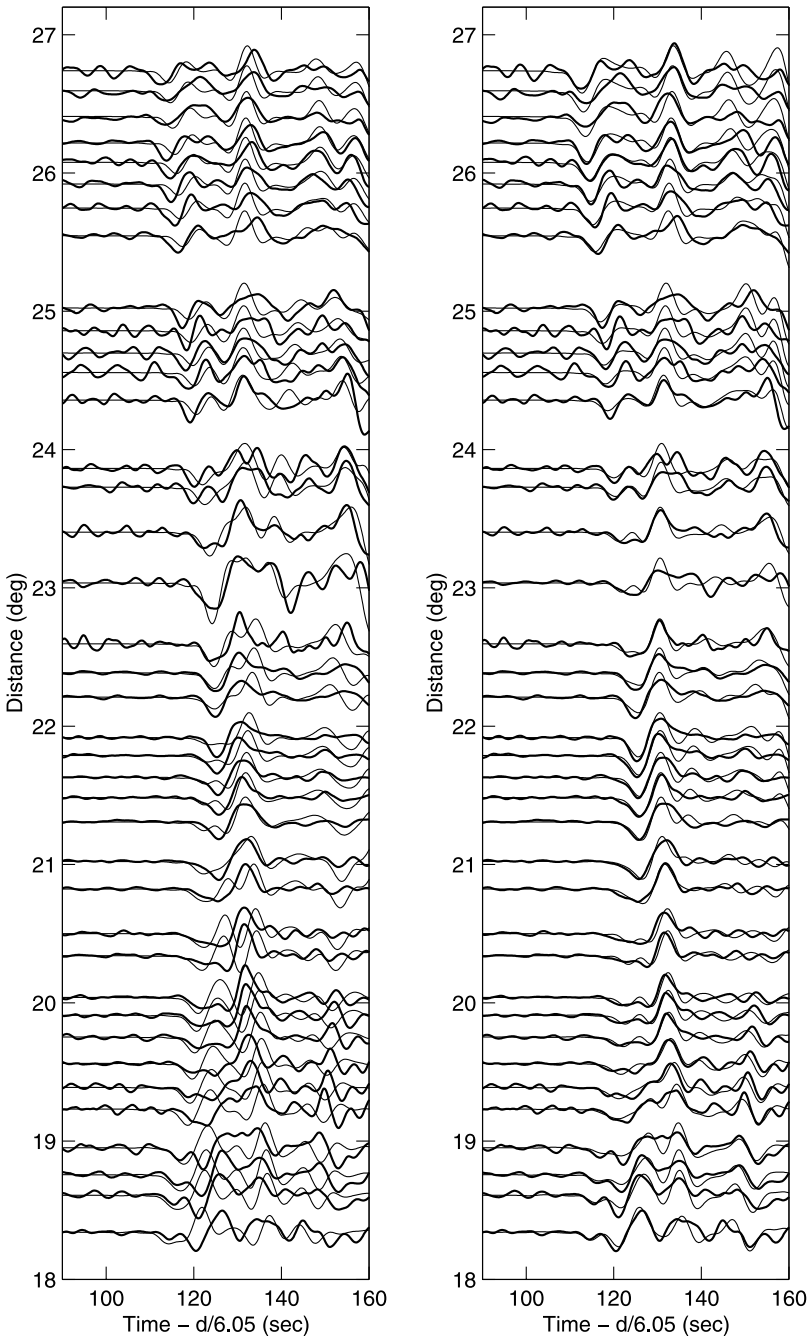

Figure 7c. Same as Figure 7a except the starting model was the low-gradient model. The heavy black lines show the data. The timescale is shown with a reduction velocity of 6.05 km s^{-1}, and d is epicentral distance in km.

where $\mathbf{d}(\mathbf{m}, r_{\text{inst}}, r_{\text{source}})$ is the updated synthetic waveform and $\mathbf{d}_{\text{obs}}$ is the observed waveform. The first-order Taylor series approximation of the term $f(\mathbf{m}_0, r_{\text{inst}}, r_{\text{source}})$ becomes

$$f(\mathbf{m}_0, r_{\text{inst}}, r_{\text{source}}) = f(\mathbf{m}, r_{\text{inst}}, r_{\text{source}}) + [\partial f/\partial \mathbf{m}](\mathbf{m}_0 - \mathbf{m}) \quad (3)$$

This gives a matrix formulation of the forward problem:

$$\Delta\mathbf{d} = [\partial f/\partial \mathbf{m}]\Delta\mathbf{m} = D\Delta\mathbf{m} \quad (4)$$

where $\Delta d = \mathbf{d} - \mathbf{d}_{\text{obs}}$ is the difference between data and synthetics and $\Delta\mathbf{m} = \mathbf{m} - \mathbf{m}_0$ is the difference between the starting model and the real model of the Earth. The term $D = [\partial f/\partial \mathbf{m}]$ is a matrix of differential seismograms which is a measurement of the sensitivity of the seismograms to the perturbations of $\mathbf{m}$ (the Earth model) for fixed events and receivers. In our inversion the differential seismograms were numerically determined by calculating synthetic seismograms for a velocity model and a perturbed model:

$$\mathbf{d}(\mathbf{m} + \delta\mathbf{m}) = \mathbf{d}(\mathbf{m}) + D\delta\mathbf{m} \quad (5)$$

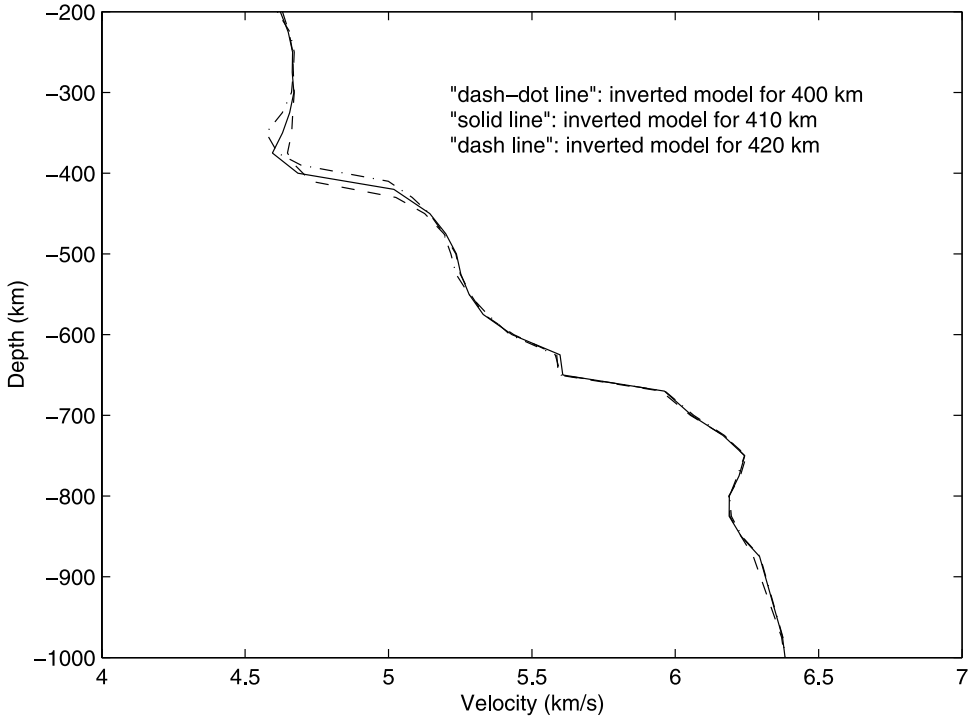

Figure 8. Three shear velocity models produced by the inversion for starting depths of the 410 km discontinuity at 400, 410, and 420 km.

where $\delta\mathbf{m}$ is a small perturbation to a model $\mathbf{m}$. We used the reflectivity method [*Fuchs and Muller*, 1971] to generate the synthetics and the differential seismograms. An advantage of generating the differential seismograms numerically is that it is easy to substitute a different synthetic technique into our code. It is clear that the solution of equation (4) depends on the starting model due to the nonlinear nature of the original problem.

[12] In this study we solve equation (4) using the conjugate gradient algorithm originally applied to seismology by *Mora* [1988] and used by *Matzel and Grand* [2004]. The conjugate gradient algorithm iteratively minimizes the misfit function

$$S(\mathbf{d},\mathbf{m}) = 1/2\left[\Delta\mathbf{d}^T C_d^{-1}\Delta\mathbf{d} + \Delta\mathbf{m}^T C_m^{-1}\Delta\mathbf{m}\right] \tag{6}$$

where C_d and C_m are the covariance matrices for data and model spaces, respectively (T indicates conjugate transpose). The algorithm for nonlinear least squares by the preconditioned conjugate gradient method is

$$\begin{aligned}
\mathbf{d}_n &= \mathbf{d}(\mathbf{m}_n)\\
\Delta\mathbf{d}_n &= \mathbf{d}_n - \mathbf{d}_{\mathrm{obs}}, \Delta\mathbf{m}_n = \mathbf{m}_n - \mathbf{m}_0\\
\mathbf{g}_n &= \partial S(\mathbf{d},\mathbf{m})/\partial\mathbf{m} = D_n^T C_d^{-1}\Delta\mathbf{d}_n + C_m^{-1}\Delta\mathbf{m}_n\\
\mathbf{c}_n &= \mathbf{p}_n + \frac{\mathbf{p}_n^T(\mathbf{g}_n - \mathbf{g}_{n-1})}{\mathbf{p}_n^T\mathbf{g}_n}\mathbf{c}_{n-1}, \quad \mathbf{c}_1 = \mathbf{p}_1, \quad (\mathbf{p}_n = C_m\mathbf{g}_n)\\
\eta_n &= \frac{\mathbf{c}_n^T\mathbf{g}_n}{\mathbf{c}_n^T D_n^T C_d^{-1} D_n\mathbf{c}_n + \mathbf{c}_n^T C_m^{-1}\mathbf{c}_n}\\
\mathbf{m}_{n+1} &= \mathbf{m}_n - \eta_n\mathbf{c}_n
\end{aligned} \tag{7}$$

for $n = 1, 2, 3, \ldots$, where $\mathbf{g}_n$ is gradient, $\mathbf{p}_n$ is preconditioning, $\mathbf{c}_n$ is conjugate direction, η_n is step length, and $\mathbf{m}_{n+1}$ is updated model. The conjugate gradient algorithm converges rapidly for upper mantle waveform problems [*Matzel*, 2002] and it iteratively minimizes the difference between data and synthetics in a least squares sense to find the local best fitting model. An intermediate solution is obtained by using the gradient vector $\partial S(\mathbf{d},\mathbf{m})/\partial\mathbf{m}$ to calculate the conjugate vector and the step length and subsequently determines the model update. Seismic synthetics are calculated by the reflectivity method [*Fuchs and Muller*, 1971]. The synthetics were calculated with 5 km thick layers but the model parameters in the inversion were average velocity over 25 km. The earthquake mechanism parameters are taken from Harvard's seismological center (centroid moment tensor solution). The source functions were derived by forward modeling seismograms in the largest distance of our data.

4. Results

[13] A difficulty with a linearized waveform inversion such as we used is that if the starting model predicts

Table 2. S Wave Misfit Function for Perturbation to Discontinuities

	410 km Discontinuity		
660 km Discontinuity	370 km	400 km	430 km
640 km	0.1452	0.1415	0.1472
670 km	0.1715	0.1384	0.1558
700 km	0.2810	0.1800	0.1615

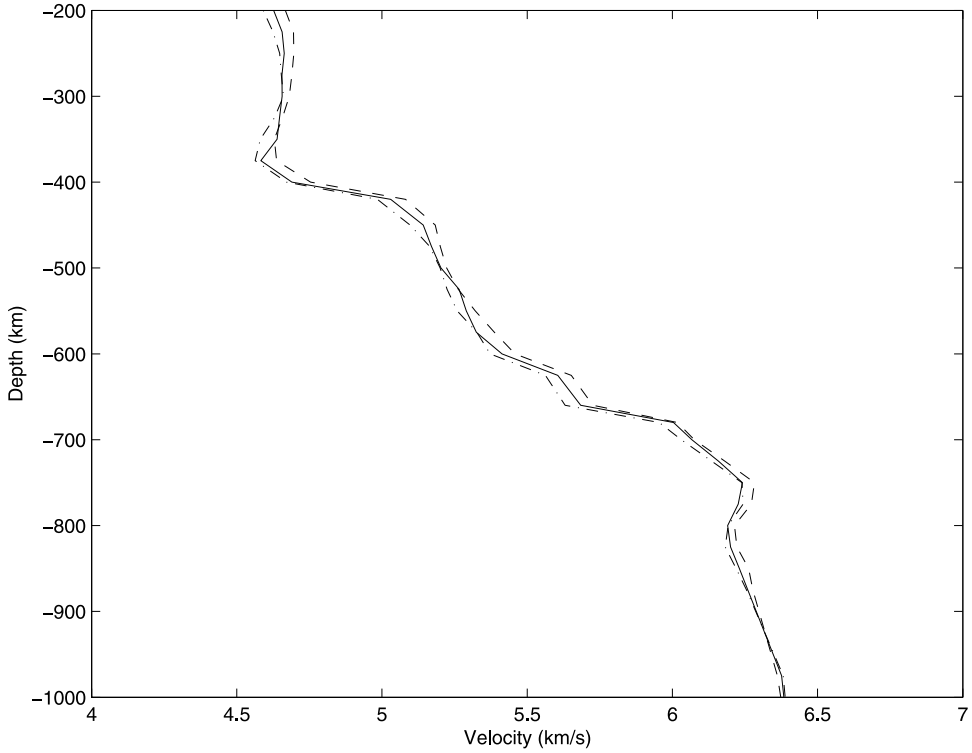

Figure 9a. Results of three inversions of the shear wave data with a +3 s shift in origin time (dashed line), a 0 shift in origin time (solid line), and a −3 s shift in origin time (dash-dotted line). The starting model in these inversions is the same as the intermediate gradient starting model in Figure 6a.

synthetics that are more than half cycle different than the data the inversion can converge to a wrong model predicting synthetics one cycle off from the data. The shear wave data have relatively stronger long-period signal than the P waves. For this reason, we initially perform the waveform inversion on the shear wave data. A second difficulty with a linearized inversion is that many local minima can exist in model space. The conjugate gradient method will find the closest local minima and thus inversion results do depend on the starting model. For this reason we attempt inversions with a range of different starting models. We set up three different starting models of shear wave velocity with different size jumps at the 410 km and 660 km discontinuities and varying gradients within the transition zone (Figure 6a). We hold the phase transition thickness to be 20 km across both discontinuities [*Melbourne and Helmberger*, 1998], although turning wave data are not strongly sensitive to discontinuity sharpness. The model with medium gradient in the transition zone is taken from *Grand and Helmberger* [1984]. The inversion results using the starting models in Figure 6a are shown in Figure 6b. It can be seen that the three different starting models produce roughly the same final models after inversion though details over 50 km depth intervals vary a little. All three models show a low-velocity zone atop the 410 km discontinuity and an unexpected high-velocity gradient beginning at a depth of about 600 km. Figures 7a, 7b, and 7c show the comparison between the observations and synthetics for different starting models and the corresponding final models. It is clear that the inversion finds a fit to the data that is much better than any of the starting models provide. The different final models, however, produce fairly similar fits to the data.

[14] We have also tested the sensitivity of the inversion results to the depths of the discontinuities in the starting model. Figure 8 shows the results of the inversion for starting models that have jumps in velocity at 400, 410, and 420 km depth. The fits to the data are similar for the three models, and indeed turning wave data are not very sensitive to the exact depth of the discontinuity. The three models all have a low-velocity zone above the 410 km discontinuity and a high gradient above the 660 km discontinuity. Table 2 shows the final misfit function for inversions using different depths for the discontinuities with a broader range than shown in Figure 8. Note discontinuity depths near 400 and 670 km depth provide better fits than using models with significantly different depth discontinuities consistent with the global average of their depths [*Flanagan and Shearer*, 1998].

[15] Finally, we also test the sensitivity of the inversions to errors in origin time of the source. Such errors would have a similar effect to errors in location. Figures 9a, 9b, and 9c show the results of inversion if the origin time is shifted 3 s faster or 3 s slower relative to the results shown above. Most of the changes due to a static time shift occur at very shallow depth. There is some change in velocity in the transition zone but they are small baseline shifts that do not change the size of discontinuities in the inversion nor the gradients. Note that the synthetic to data fits are as good as shown in Figures 7a, 7b, and 7c.

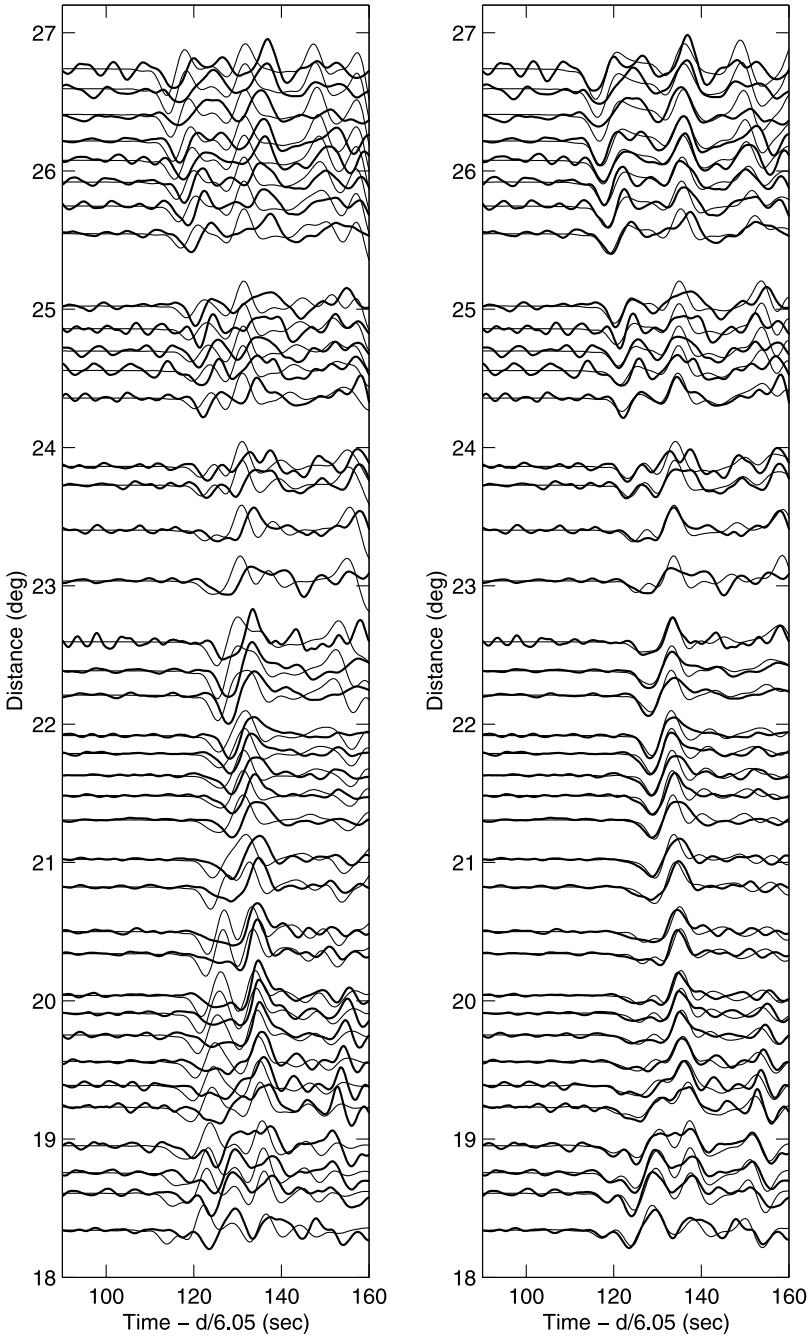

Figure 9b. Data and synthetic match for the +3 s shifted data. (left) Synthetics computed using the starting model and (right) synthetics computed using the inverted model. The heavy black lines show the data. The timescale is shown with a reduction velocity of 6.05 km s^{-1}, where d is epicentral distance in km.

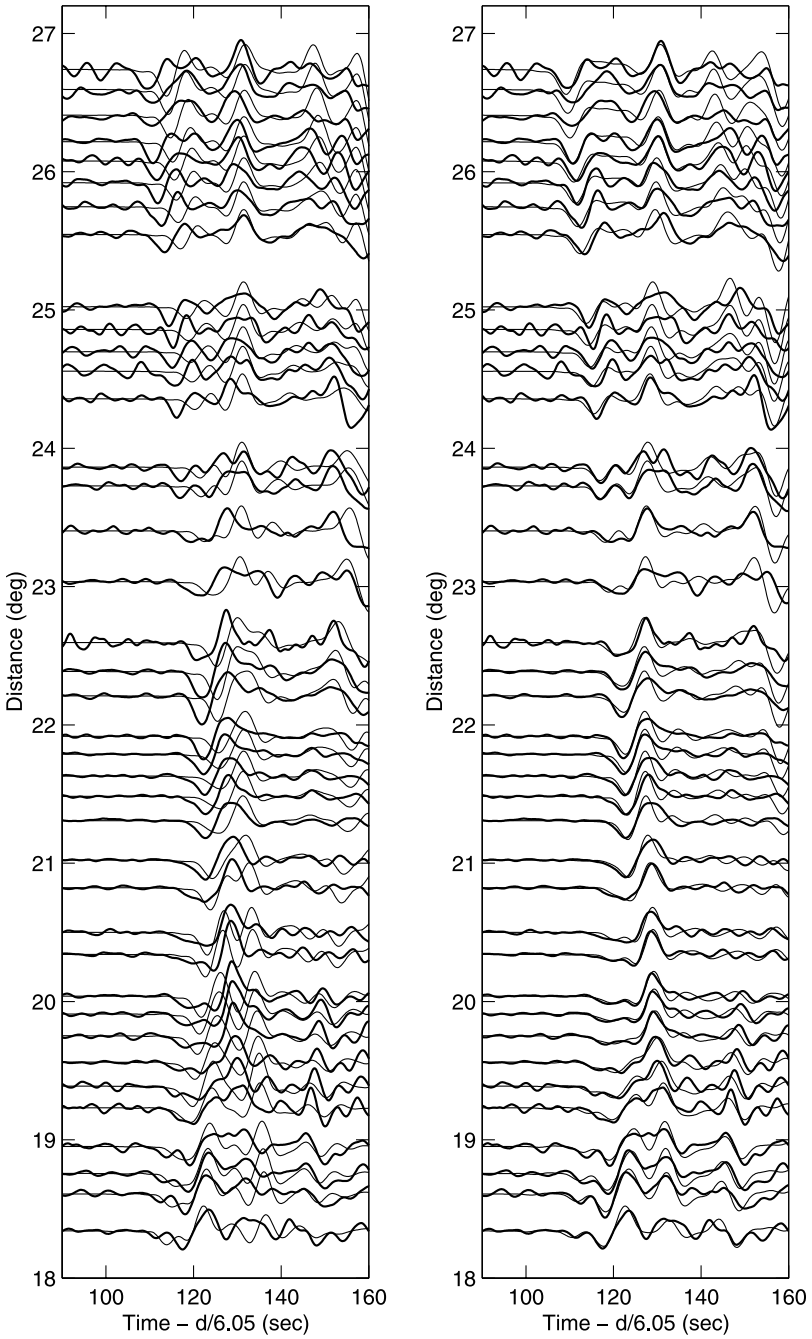

Figure 9c. Data and synthetic match for the −3 s shifted data. (left) Synthetics computed using the starting model and (right) synthetics computed using the inverted model. The heavy black lines show the data. The timescale is shown with a reduction velocity of 6.05 km s^{-1}, where d is epicentral distance in km.

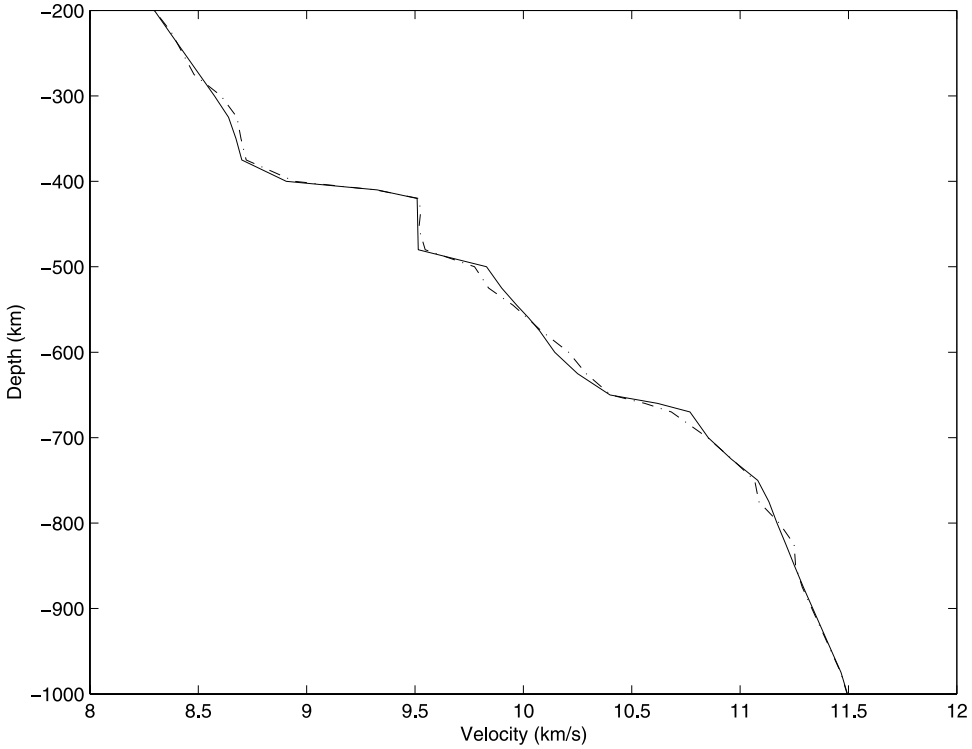

Figure 10a. Starting and final models for inversion of the P data. The solid line is the starting model.

[16] The compressional wave seismograms have weak long-period signal relative to noise level. At frequencies near 1 Hz, however, the amplitude is well above noise level so we chose to invert the P wave data with a higher passband (up to 1.5 Hz). Although there may be other earthquakes with stronger P waves the advantage to modeling both P and S for the same earthquake is that origin time errors, earthquake location errors, and the volume of mantle sampled by the two types of waves are identical so that the P and S models can be compared directly.

[17] The initial starting model used for the compressional waveform inversion was model S25 [*LeFevre and Helmberger*, 1989]. At the high frequencies present in the P data we were required to forward model the data until the timing was almost correct in order for the inversion to converge properly. The P data also showed an extra triplication in the data at close distances (Figure 5). This extra triplication required a discontinuity within the transition zone to model. We found by forward modeling a model that mimicked the features found in the shear, except for the addition of a small jump in velocity near 490 km depth that also matched the traveltimes of the P data. We used that model as the starting model in our inversion of the P data. Figures 10a and 10b show the results of the waveform inversion for the compressional wave observations with model comparisons (starting and final) and waveform comparisons. Two main discontinuities at 410 km and 660 km and a small jump at a depth of 490 km can be observed in the upper mantle. The small jump at 490 km in our model accounts for the two low-amplitude phases that merge together with increasing distance (observed from 18.5° to 19.5°, see Figure 5). From Figure 10a it is evident that the low-velocity zone atop the 410 km discontinuity in the compressional velocity model is not as significant as the feature observed in the shear velocity model. Also, the S inversion results showed no discontinuity near 490 km depth. To make the P and S models more compatible in major features, we ran an inversion of the S wave data including a small jump in velocity at 490 km depth. The results are shown in Figures 11a and 11b. It can be seen in Figures 11a and 11b that the inversion of the S data tends to diminish the size of any jump in velocity near 490 km depth but does not eliminate the jump. The fit of the shear wave data by the model shown in Figures 11a and 11b is essentially as good as the fits to the data in Figure 6.

5. Discussion

[18] The final models for the P and S velocity beneath eastern Mexico are shown compared to the PREM and IASPEI models in Figure 12. Note that for both P and S waves, there appears to be a far larger jump at 410 km depth in our models than either of the global average models, although the low-velocity zone above the 410 km discontinuity makes it ambiguous to define exactly what the jump at 410 km is. We take the total velocity increase over 20 km depth to define the discontinuity size. In our models, we find an increase of 6.2% for P waves and 7.3% for S waves at 410 km depth and an increase of 3.3% for P waves and 6.3% for S waves at 660 km depth. For comparison, PREM has a P jump of 3.4% and an S jump of 4.2% at 410 km depth and a P jump of 5% and an S jump of 7% at 660 km depth. If we use the elasticity data of *Sinogeikin et al.* [1998] for olivine and its high-pressure polymorphs then the

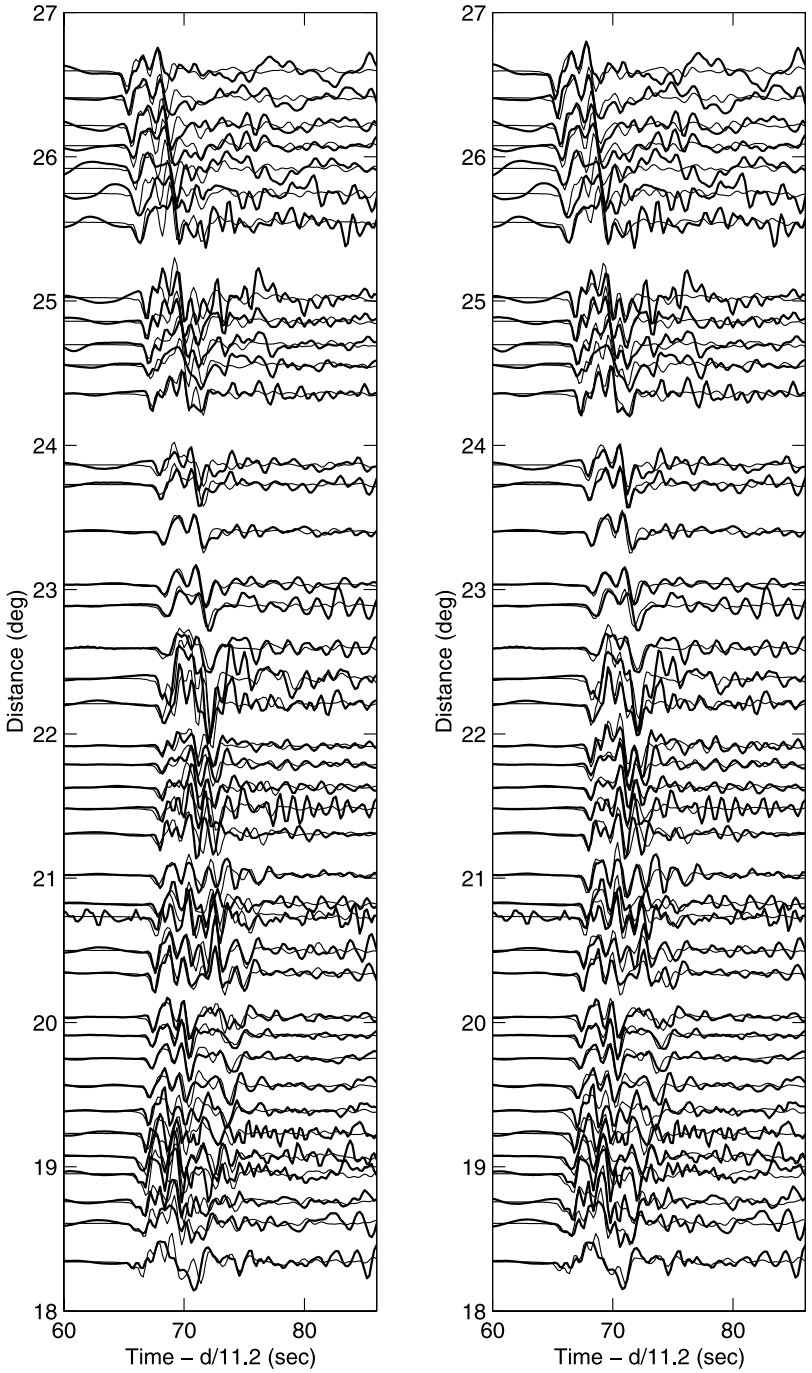

Figure 10b. P wave data and synthetics. (left) Synthetics computed using the starting model and (right) synthetics computed using the inverted model. The heavy black lines show the data. The timescale is shown with a reduction velocity of 11.2 km s^{-1}, where d is epicentral distance in km.

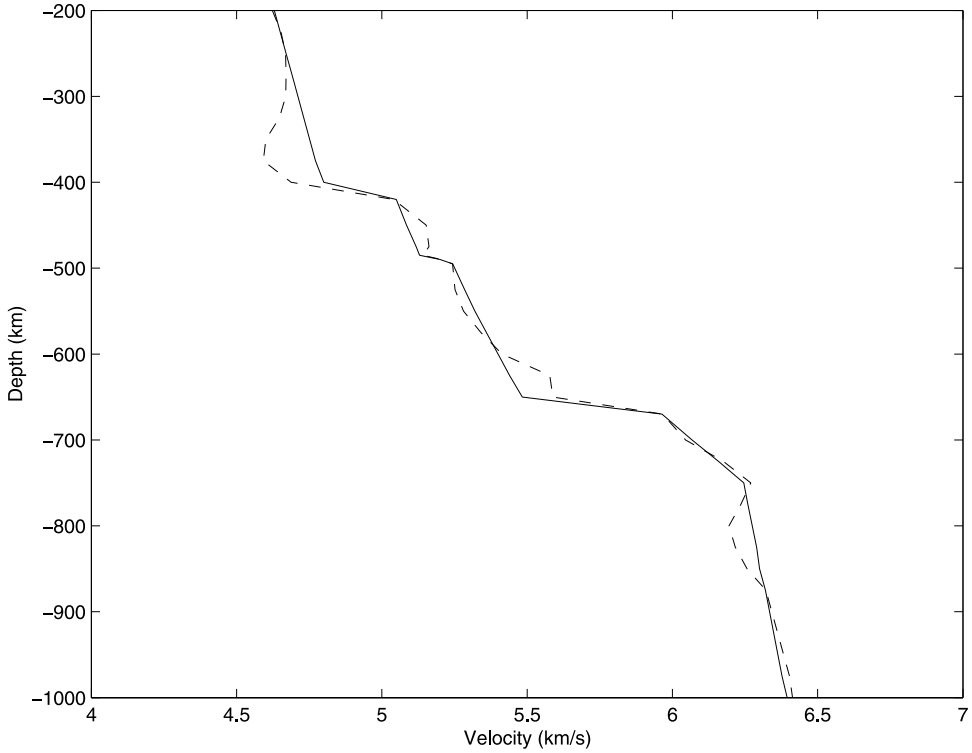

Figure 11a. Results of inversion of the shear wave data when a small discontinuity was added at 490 km depth in the starting model. The starting model is the solid line.

P and S velocity jumps at 410 km depth imply 65% olivine, respectively, for the mantle beneath eastern Mexico. These values are high even with respect to the pyrolite model but the low-velocity zone above the 410 km discontinuity in our model (discussed below) may result in an over estimate of the olivine content when using single crystal mineral physics estimates for what the jump should be. The jumps across 660 km for P and S waves imply an olivine content of 45% and 52.5%, respectively, using the results of *Sinogeikin et al.* [2003] and are less than that of a pyrolite composition. The comparison of models in Figure 12 clearly shows a relatively small jump in P velocity near 660 km relative to other standard models. In Figures 13a and 13b we show a comparison of P data and synthetics for an altered model with a larger jump (5%) in velocity at 660 km depth. Note the greater misfit between data and synthetics for this model as compared to our preferred model (Figures 10a and 10b). For the profile examined here the jump in velocity at 660 km depth for P waves must be smaller than in the standard models. Our results are also consistent with the results of *Shearer and Flanagan* [1999] and *Estabrook and Kind* [1996], who found far smaller jumps in P velocity at 660 km depth than the PREM model and also found an inconsistency between their seismic results for P wave velocity jump at 660 km depth and predictions for the pyrolite model. Our final models also have a small discontinuity near 490 km depth in P and S. Some jump in P velocity near that depth is required to fit the double arrivals shown in Figure 5, but there is no clear triplication in the S data that require such a feature. In fact, inversion of the S data with a small jump near 490 km depth tends to minimize the jump. We thus are not confident about the size of this discontinuity, although from the P wave data it appears that some small feature exists. This discontinuity is likely the same feature imaged by *Shearer* [1990, 1993] and may be due to the β to γ phase transition in olivine.

[19] With respect to the size of the upper mantle discontinuities, it appears that the jump in velocity for both P and S waves is larger at 410 km depth than is given in standard models such as PREM and IASPEI. The jumps we find tend to favor a more olivine rich mantle similar to pyrolite than the standard seismic models would imply. On the other hand, we find the P jump at 660 km depth appears to be too small for an olivine rich mantle. The region we have sampled likely has a cold transition zone based on the tomography model of *Van der Lee and Nolet* [1997]. They find higher than average shear velocities from 550 to 650 km depth in eastern Mexico and identify this feature with remnants of the Farallon plate that subducted roughly 30 Ma. It may be that the deep transition zone under eastern Mexico has a chemical anomaly associated with subducted slab; for example, a layer of eclogite rich mantle ponded near the 660 km depth discontinuity as proposed by *Ringwood and Irifune* [1988]. Further detailed studies of the transition zone in other regions will likely be required before definitive conclusions can be drawn with regard to a change in major element chemistry in the deep transition zone.

[20] Two other unusual features appear in our shear model shown in Figures 11a and 11b. The first is a low-velocity zone just above the 410 km discontinuity and the second is a jump in velocity of 2.4% at about 600 km depth, well above the 660 km discontinuity. Neither of these features are strong in the P model and both may be related

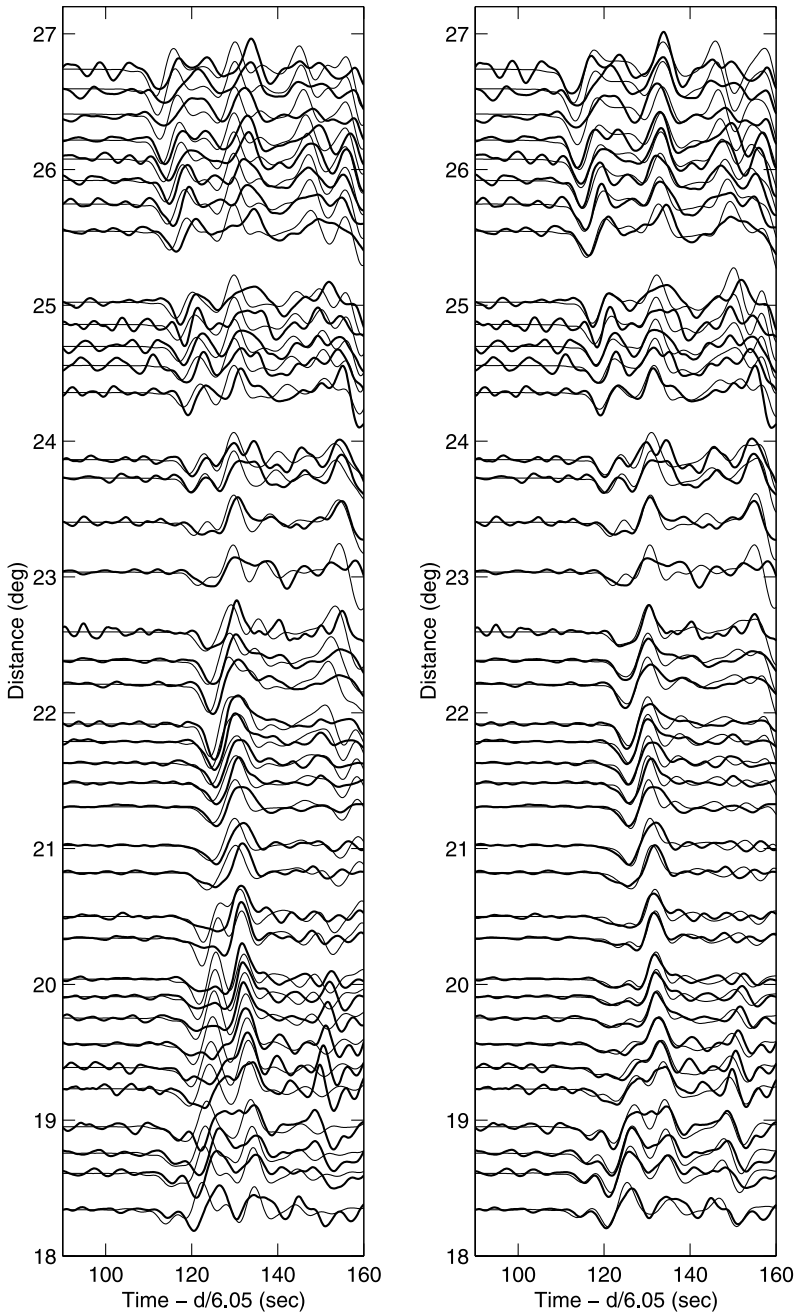

Figure 11b. A comparison of data and synthetics using the starting model in Figure 11a (left) and using the inverted model in Figure 11a (right). The heavy black lines show the data. The timescale is shown with a reduction velocity of 6.05 km s^{-1}, where d is epicentral distance in km.

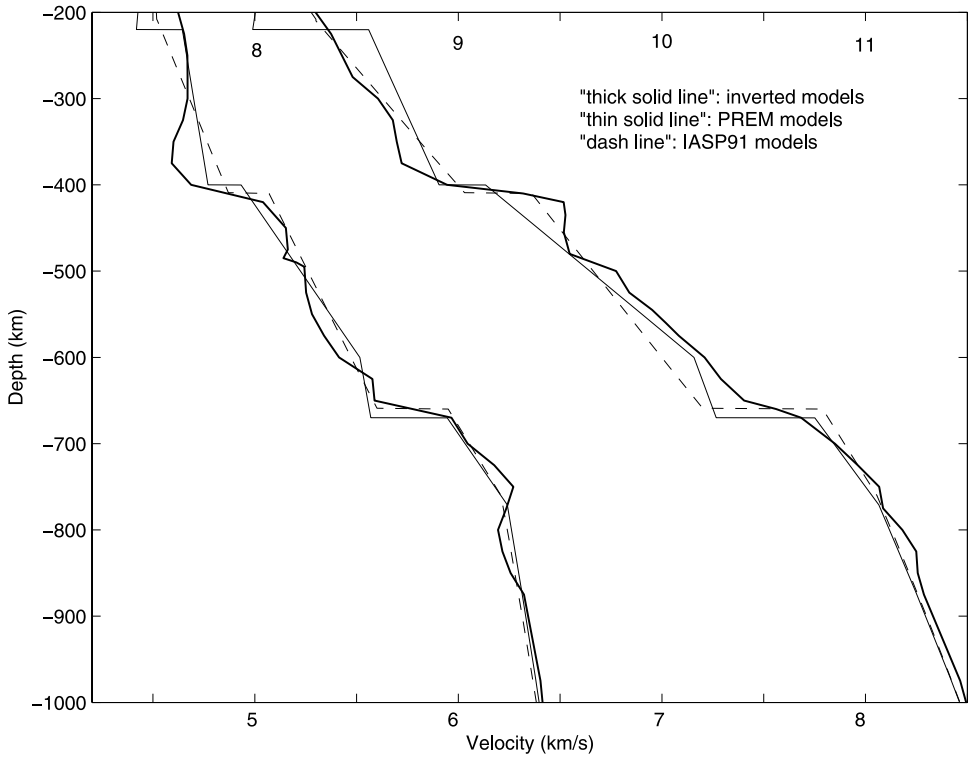

Figure 12. Comparison of the final inverted models for P and S velocity to the IASPEI model and PREM model.

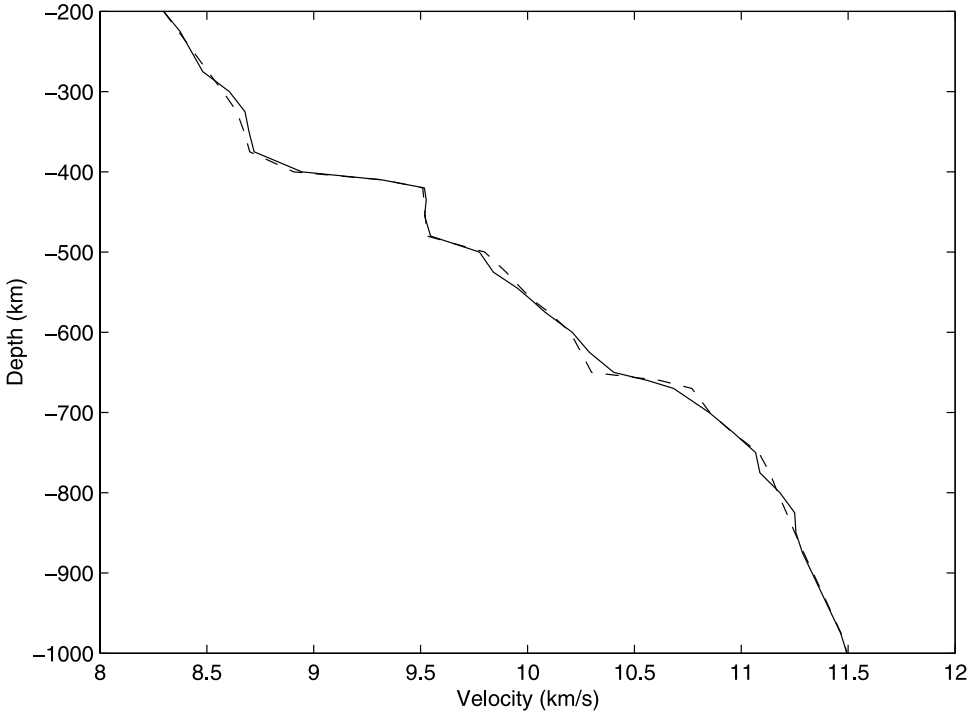

Figure 13a. A modification of our preferred P model that matches traveltimes but has a larger jump in velocity at 660 km depth (5%). The solid line is the preferred model shown in Figures 10a and 10b.

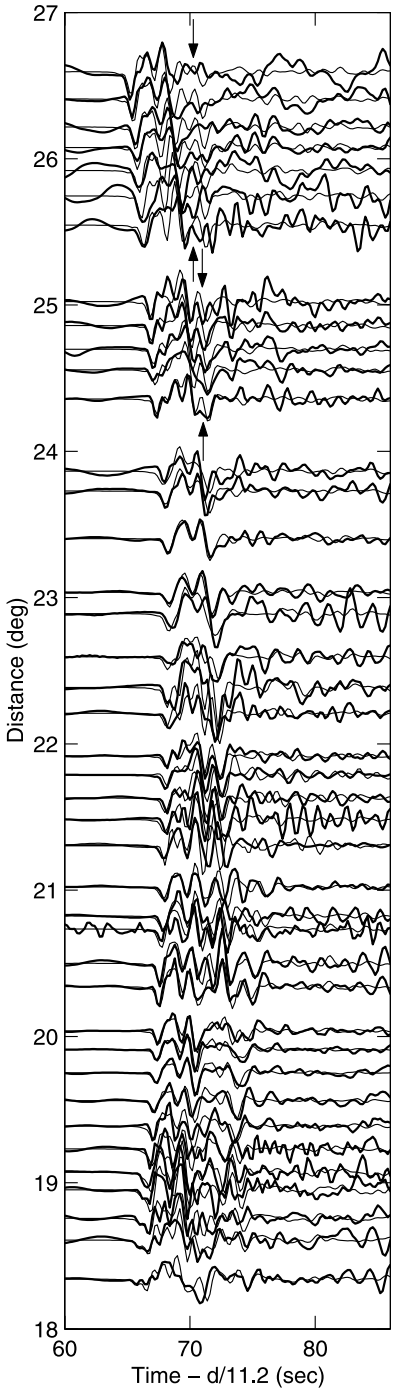

Figure 13b. Comparison of P data and synthetics calculated using the modified P model shown in Figure 13a. Arrows indicate misfits in the waveforms that are worse than for our preferred model, and the heavy black lines show the data. The timescale is shown with a reduction velocity of 11.2 km s^{-1}, where d is epicentral distance in km.

to subducted slab stagnant in the mantle transition zone. The high-velocity jump near 600 km depth may be due to cold slab material laying on the 660 km transition zone as proposed by *Van der Lee and Nolet* [1997]. *Cammarano et al.* [2003] estimated about a 0.8% change in shear velocity per 100°C change in temperature at depths near 600 km. The jump we observe of 2.4% at 600 km would imply a change in temperature of 300°C associated with the slab. This is larger than the estimated 200°C thermal anomaly estimated by *Van der Lee and Nolet* [1997] for the Farallon plate 26 Myr after subduction. Thus, although the high gradient we observe at 600 km depth is likely due to the cold temperatures within a stagnant slab, it appears that temperature alone is not sufficient to explain this feature. Perhaps this is again an indication of chemical heterogeneity just above the 660 km discontinuity or to a relatively sharp phase transition within a cold transition zone.

[21] The second unusual feature in our model that may be related to subduction processes is a low-velocity zone above the 410 km discontinuity, more prominent in the S model than the P model. Such a feature has been found in previous studies as well. *Revenaugh and Sipkin* [1994] were the first to find a low-velocity zone above 400 km depth in their ScS reverberation study of north China. They interpreted the feature as a zone of partial melting due to volatiles released by the subducting Pacific plate which is presently beneath the low-velocity zone. *Nolet and Zielhuis* [1994] found low shear velocities beneath the Tornquist-Teisseyre zone from 300 to 500 km depth. They interpreted this anomaly as a region with higher water content than normal and postulated the water was introduced by subduction. More recently, *Vinnik et al.* [2003] and *Song et al.* [2004] have also found evidence of a low-velocity zone near 400 km depth. Both of those studies were in regions where plate convergence has occurred during the past 50 Myr. We test the resolution of our model with respect to the low-velocity zone seen in our model by running inversions for the S data where the gradient from 200 to 400 km is constrained to be linear. Figure 14 shows the starting model and the results of the inversion. Figure 15 shows the data to synthetic match for the model shown in Figure 14. Note that there is significant mismatch between data and synthetics at distances from 18° to 20° for this model and that the inversions that have a low-velocity zone above 410 km depth provide much better fits to the data (Figures 7a, 7b, and 7c). We ran other inversions with different starting gradients from 200 to 400 km depth and found that the best fitting model with a linear gradient from 200 to 400 km depth had a slightly negative gradient. Thus we conclude that the low-velocity zone atop the 410 km discontinuity is a robust feature of the upper mantle beneath eastern Mexico.

[22] Recently, *Bercovici and Karato* [2003] hypothesized that water rich mantle could cause melting above the 410 km discontinuity but not below. This is due to the higher compatibility of water in transition zone minerals as opposed to olivine as well as the fact that the density of melt near 400 km depth is thought to be greater than the matrix. The fact that we find a far stronger low-velocity zone in S than in P is supportive of the low-velocity zone being due to partial melt that is likely due to the presence of water or other volatiles introduced in some way by subduction to the west.

6. Conclusions

[23] The seismic structure of the upper mantle beneath eastern Mexico is investigated using triplicated waveform

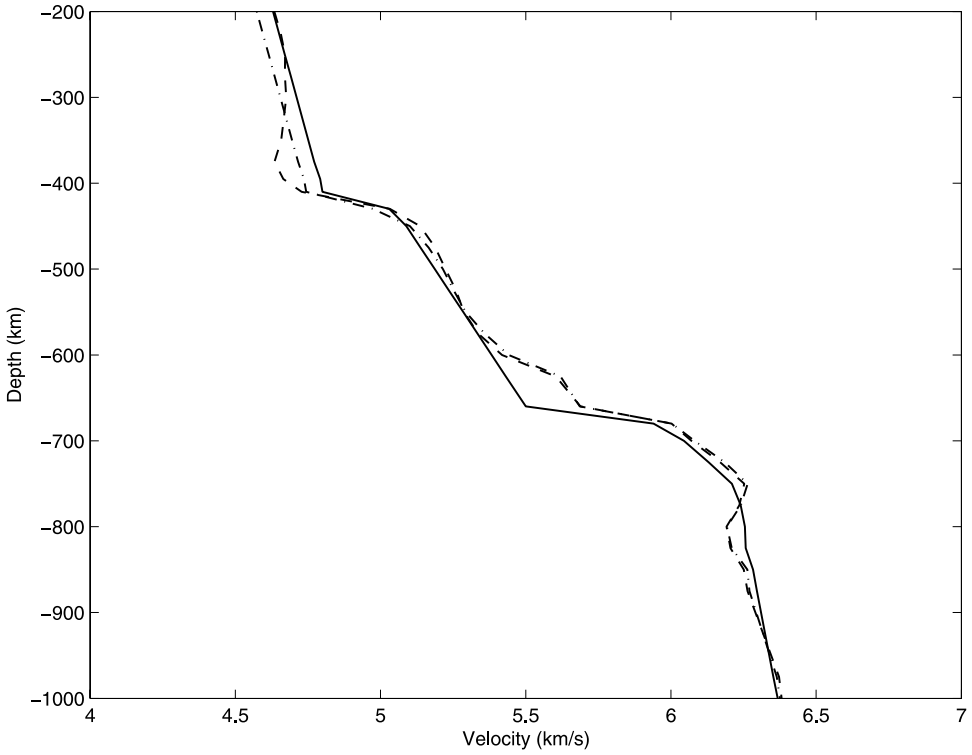

Figure 14. Results of inverting the S data with a constraint that there be a linear gradient from 200 to 400 km depth. The solid line shows the starting model. Our preferred model (dashed line) with a low-velocity zone above 410 km depth is also shown.

observations recorded by the 950 km long La Ristra seismic array. We applied a waveform inversion technique to one of the most densely spaced coincident P and S profiles studied to date. The compressional and shear wave observations are produced by a common earthquake that occurred at the border of Mexico and Guatemala. Our results reveal that there is a 50 km thick low-velocity zone atop the 410 km discontinuity, which is more prominent in the shear velocity model than in the compressional velocity model. The best fitting models in this study region have velocity increases of 6.2% for compressional velocity and 7.3% for shear velocity across the 410 km discontinuity. Across the 660 km discontinuity, we find velocity jumps of 3.3% for P wave velocity and 6.3% for S wave velocity. These models show significantly larger velocity increases across the 410 km discontinuity than the PREM and IASPEI models. Our results also show that the velocities in our compressional velocity model within the transition zone are significantly larger than those in the standard models (see Figure 12). In addition, there is a small jump near 490 km.

[24] From the size of the jumps across the discontinuities, the olivine content can be estimated for the upper mantle. In this study, the velocity increases across the discontinuities imply that the olivine content is 65% at the 410 km and 45% and 52.5% at the 660 km discontinuity for the compressional and shear wave models, respectively. At face value, these results show that the content of olivine in the upper mantle beneath eastern Mexico changes with depth within the transition zone. This may be due to the presence of a subducted slab stagnant above the 660 km discontinuity. The shallower mantle compositions inferred are closer to pyrolite than standard upper mantle seismic models imply but because of the low-velocity zone above the 410 km discontinuity it may not be proper to use single crystal mineral physics results to interpret the velocity change across 410 km depth purely in terms of the values observed in the olivine to wadsleyite phase transition. Future work should begin to do joint inversions of seismic data and mineral physics data to place better constraints on the mineralogy and chemical composition of the upper mantle.

[25] The transition zone of the upper mantle beneath eastern Mexico is likely to have had subducted lithosphere enter it within the last 30 Myr. Tomography also shows that it may be a location where slab is stagnant above the 660 km discontinuity. Given this tectonic regime, we interpret the low-velocity zone beneath eastern Mexico to be due to partial melting of a dense silicate layer caused by water release associated with the subduction of the Farallon or Cocos plate into the transition zone. We conclude that the difference between P and S velocity jumps at the 660 km discontinuity and the difference of the olivine content between the 410 km and 660 km discontinuities possibly results from chemical heterogeneity generated by the stagnation of the subducted plate near the 660 km discontinuity.

[26] We have interpreted some unusual features in our models in terms of the effect of subduction. It is unclear, however, how ubiquitous a low-velocity zone atop the 410 km discontinuity is or how common are high gradients near 600 km depth. With the advent of large temporary deployments of broad band seismometers more detailed

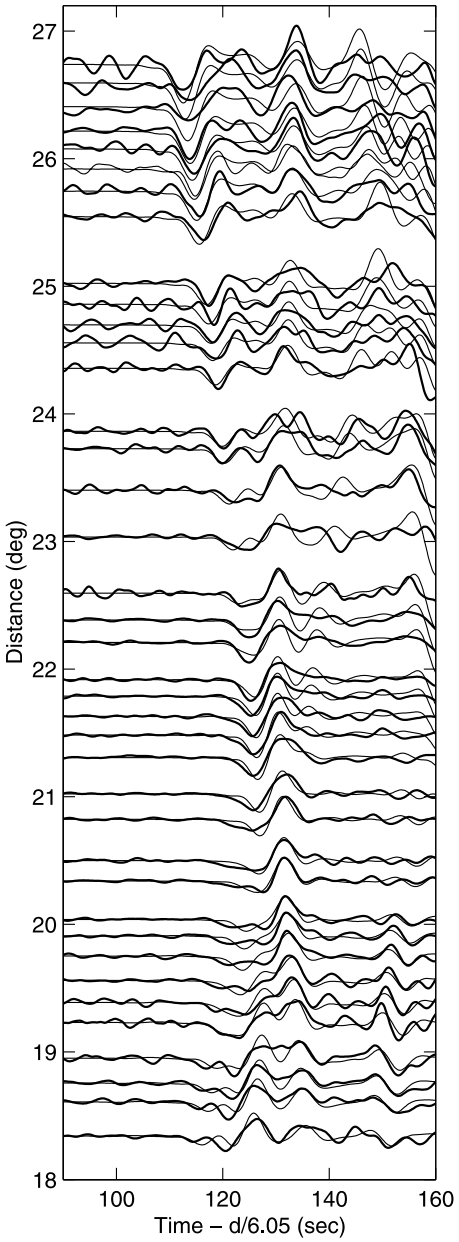

Figure 15. Shear wave data and synthetics. The synthetics are computed using the model shown in Figure 14 where a constraint is imposed that there is a linear gradient from 200 to 410 km depth. The heavy black lines show the data. The timescale is shown with a reduction velocity of 6.05 km s^{-1}, where d is epicentral distance in km.

regional studies of the upper mantle transition zone should be possible in many tectonic environments. The results of such studies should lead to better constrained interpretations of the seismic models and thus a better understanding of the mineralogy and dynamics of the upper mantle.

[27] **Acknowledgments.** We thank the Geology Foundation of the Jackson School of Geosciences at the University of Texas for support during the course of this work. We also thank Jay Bass for helpful discussions on upper mantle composition and phase transitions and Peter Shearer and Don Helmberger for useful reviews of the manuscript. This research was supported by NSF through grant EAR-0112256.

References

Bass, J. D., and D. L. Anderson (1984), Composition of the upper mantle: Geophysical tests of two petrological models, *Geophys. Res. Lett.*, *11*, 237–240.

Bercovici, D., and S. Karato (2003), Whole mantle convection and the transition zone water filter, *Nature*, *425*, 39–44.

Bina, C. R., and G. Helffrich (1994), Phase transition Claperon slopes and transition zone seismic discontinuity topography, *J. Geophys. Res.*, *99*, 15,853–15,860.

Bina, C. R., and B. J. Wood (1984), The eclogite to garnetite transition: Experimental and thermodynamic constraints, *Geophys. Res. Lett.*, *11*, 955–958.

Bina, C. R., and B. J. Wood (1987), Olivine-spinel transitions: Experimental and thermodynamic constraints for the nature of the 410 km seismic discontinuity, *J. Geophys. Res.*, *92*, 4853–4866.

Cammarano, F., S. Goes, P. Vacher, and D. Giardini (2003), Inferring upper mantle temperatures from seismic velocities, *Phys. Earth Planet. Inter.*, *138*, 197–222.

Cammarano, F., S. Goes, A. Deuss, and D. Giardini (2005), Is a pyrolite mantle compatible with seismic data?, *Earth Planet. Sci. Lett.*, *232*, 227–243.

Deuss, A., and J. Woodhouse (2001), Seismic observations of splitting of the mid-transition zone discontinuity in the Earth's mantle, *Science*, *294*, 354–357.

Dziewonski, A., and D. Anderson (1981), Preliminary reference Earth model, *Phys. Earth Planet. Inter.*, *25*, 297–356.

Estabrook, C. H., and R. Kind (1996), The nature of the 660–kilometer upper-mantle seismic discontinuity from precursors to the PP phase, *Nature*, *274*, 1179–1182.

Flanagan, M. P., and P. M. Shearer (1998), Global mapping of topography on transition zone velocity discontinuities by stacking SS precursors, *J. Geophys. Res.*, *103*, 2673–2692.

Fuchs, K., and G. Muller (1971), Computation of synthetic seismograms with the reflectivity method and comparison with observations, *Geophys. J. R. Astron. Soc.*, *23*, 417–433.

Gao, W., S. P. Grand, W. S. Baldridge, D. Wilson, M. West, J. F. Ni, and R. Aster (2004), Upper mantle convection beneath the central Rio Grande rift imaged by P and S wave tomography, *J. Geophys. Res.*, *109*, B03305, doi:10.1029/2003JB002743.

Grand, S. P. (2002), Mantle shear wave tomography and the fate of subducted slabs, *Philos. Trans. R. Soc. London, Ser. A*, *360*, 2475–2491.

Grand, S. P., and D. Helmberger (1984), Upper mantle shear structure of North America, *Geophys. J. R. Astron. Soc.*, *76*, 399–438.

Gu, Y., A. M. Dziewonski, and G. Ekstrom (2003), Simultaneous inversion for mantle velocity and topography of transition zone discontinuities, *Geophys. J. Int.*, *154*, 559–583.

Helffrich, G. R., E. Asencio, J. Knapp, and T. Owens (2003), Transition zone structure in a tectonically inactive area: 410 and 660 km discontinuity properties under the northern North Sea, *Geophys. J. Int.*, *155*, 193–199.

Kennett, B. L. N., and E. R. Engdahl (1991), Traveltimes for global earthquake location and phase identification, *Geophys. J. Int.*, *105*, 429–465.

Kennett, B. L. N., E. R. Engdahl, and R. Buland (1995), Constraints on seismic velocities in the Earth from travel times, *Geophys. J. Int.*, *122*, 108–124.

LeFevre, L. V., and D. V. Helmberger (1989), Upper mantle P velocity structure of the Canadian shield, *J. Geophys. Res.*, *94*, 17,749–17,765.

Li, B. (2003), Compressional and shear wave velocities of ringwoodite γ-Mg_2SiO_4 to 12 GP, *Am. Mineral.*, *88*, 1312–1317.

Li, B., Y. R. C. Liebermann, and D. J. Weidner (1998), Elastic moduli of wadsleyite (β-Mg_2Sio_4) to 7 gigapascals and 873 kelvin, *Science*, *281*, 675–677.

Masters, T. G., G. Laske, H. Bolton, and A. Dziewonski (2000), The relative behavior of shear velocity, bulk sound speed, and compressional velocity in the mantle: Implications for chemical thermal structure, in *Earth's Deep Interior: Mineral Physics and Tomography From the Atomic to the Global Scale*, *Geophys. Monogr. Ser.*, vol. 117, edited by S. Karato et al., pp. 63–87, AGU, Washington, D. C.

Matzel, E. (2002), The anisotropic seismic structure of the Earth's mantle: Investigations using full waveform inversion, dissertation, Univ. of Tex. at Austin, Austin.

Matzel, E., and S. P. Grand (2004), The anisotropic seismic structure of the East European platform, *J. Geophys. Res.*, *109*, B01302, doi:10.1029/2001JB000623.

Megnin, C., and B. Romanowicz (2000), The three-dimensional shear velocity structure of the mantle from the inversion of body, surface and higher-mode waveforms, *Geophys. J. Int.*, *143*, 709–728.

Melbourne, T., and D. V. Helmberger (1998), Fine structure of the 410 km discontinuity, *J. Geophys. Res.*, *103*, 10,091–10,102.

Mora, P. (1988), Elastic wave-field inversion of reflection and transmission data, *Geophysics*, *53*(6), 750–759.
Nolet, G., and A. Zielhuis (1994), Low S velocities under the Tornquist-Teisseyre zone: Evidence for water injection into the transition zone by subduction, *J. Geophys. Res.*, *99*, 15,813–15,820.
Nolet, G., S. P. Grand, and B. L. N. Kennett (1994), Seismic heterogeneity in the upper mantle, *J. Geophys. Res.*, *99*, 23,753–23,766.
Revenaugh, J., and S. A. Sipkin (1994), Seismic evidence for silicate melt atop the 410–km mantle discontinuity, *Nature*, *369*, 474–476.
Ringwood, A. E. (1975), *Composition and Petrology of the Earth's Mantle*, McGraw-Hill, New York.
Ringwood, A. E., and T. Irifune (1988), Nature of the 650–km seismic discontinuity: Implications for mantle dynamics and differentiation, *Nature*, *331*, 131–136.
Ritsema, J., H. J. van Heijst, and J. H. Woodhouse (1999), Complex shear wave velocity structure imaged beneath Africa and Iceland, *Science*, *286*, 1925–1928.
Romanowicz, B. (1991), Seismic tomography of the Earth's mantle, *Annu. Rev. Earth Planet. Sci.*, *19*, 77–99.
Ryberg, T., F. Wenzel, A. V. Egorkin, and L. Solodilov (1997), Short-period observation of the 520 km discontinuity in the northern Eurasia, *J. Geophys. Res.*, *102*, 5413–5422.
Shearer, P. M. (1990), Seismic imaging of upper-mantle structure with new evidence for a 520-km discontinuity, *Nature*, *344*, 121–126.
Shearer, P. M. (1993), Global mapping of upper mantle reflectors from long-period SS precursors, *Geophys. J. Int.*, *115*, 878–904.
Shearer, P. M., and M. P. Flanagan (1999), Seismic velocity and density jumps across the 410- and 660-kilometer discontinuities, *Science*, *285*, 1545–1548.
Simmons, N. A., and H. Gurrola (2000), Multiple seismic discontinuities near the base of the transition zone of the Earth's mantle, *Nature*, *405*, 559–562.
Sinogeikin, S. V., T. Katsura, and J. D. Bass (1998), Sound velocities and elastic velocities of Fe-bearing wadsleyite and ringwoodite, *J. Geophys. Res.*, *103*, 20,819–20,825.
Sinogeikin, S. V., J. D. Bass, and T. Katsura (2003), Single-crystal elasticity of ringwoodite to high pressure and high temperatures: Implications for 520 km seismic discontinuity, *Phys. Earth. Planet. Inter.*, *136*, 41–66.
Song, T., D. Helmberger, and S. P. Grand (2004), Low-velocity zone atop the 410-km seismic discontinuity in the northwestern United States, *Nature*, *427*, 530–533.
Tajima, F., and P. Grand (1995), Evidence of high velocity anomalies in the transition zone associated with southern Kurile subduction zone, *Geophys. Res. Lett.*, *22*, 3139–3142.
Tajima, F., and P. Grand (1998), Variation of transition zone high-velocity anomalies and depression of 660 km discontinuity associated with subduction zones from the southern Kuriles to Izu-Bonin and Ryukyu, *J. Geophys. Res.*, *103*, 15,015–15,036.
Van der Lee, S., and G. Nolet (1997), Seismic image of the subducted trailing fragments of the Farallon plate, *Nature*, *386*, 266–269.
Vinnik, L., M. R. Kumar, R. Kind, and V. Farra (2003), Super-deep low-velocity layer beneath the Arabian plate, *Geophys. Res. Lett.*, *30*(7), 1415, doi:10.1029/2002GL016590.
Walck, M. C. (1984), The P-wave upper mantle structure beneath an active spreading center–the Gulf of California, *Geophys. J. R. Astron. Soc.*, *76*, 697–723.
Weidner, D. J. (1985), Mineral physics test of a pyrolite mantle, *Geophys. Res. Lett.*, *12*, 417–420.
Wilson, D., R. Aster, J. Ni, S. Grand, M. West, W. Gao, W. S. Baldridge, and S. Semken (2005), Imaging the seismic structure of the crust and upper mantle beneath the Great Plains, Rio Grande Rift, and Colorado Plateau using receiver functions, *J. Geophys. Res.*, *110*, B05306, doi:10.1029/2004JB003492.

W. Gao and S. P. Grand, Jackson School of Geosciences, University of Texas at Austin, 1 University Station C1100, Austin, TX 78712, USA. (weigao@mail.utexas.edu)
E. Matzel, Lawrence Livermore National Laboratory, L-206, 7000 East Avenue, Livermore, CA 94550, USA.